energies

MDPI

Article

Intelligent Unified Power Quality Conditioner with Reactive Power Sharing for Improving DC-Link Voltage and Power Quality

Kuang-Hsiung Tan [1,*], Faa-Jeng Lin [2], Cheng-Ming Shih [2], Wei-Ming Lu [2], Pei-Chen Tsai [2] and Chia-Ching Lin [3]

[1] Department of Electrical and Electronic Engineering, National Defense University, Taoyuan 335, Taiwan
[2] Department of Electrical Engineering, National Central University, Zhongli 320, Taiwan; linfj@ee.ncu.edu.tw (F.-J.L.); 114581002@cc.ncu.edu.tw (C.-M.S.); 113521055@cc.ncu.edu.tw (W.-M.L.); 114521061@cc.ncu.edu.tw (P.-C.T.)
[3] R&D Center, Fortune Electric Co., Ltd., Zhongli 320, Taiwan; jackylin@fortune.com.tw
* Correspondence: s913115@gmail.com; Tel.: +886-3-3809991 (ext. 128)

Abstract

A three-phase, four-leg intelligent unified power quality conditioner (UPQC) is proposed to mitigate grid voltage distortions, grid current total harmonic distortion (THD), current unbalance, and lagging power factor (PF). The developed UPQC possesses the reactive power sharing capability to share the load reactive power demand between the series and shunt inverters. Moreover, when grid voltage distortions or sudden load changes occur, the power mismatch between the series and shunt inverters of the UPQC can result in DC-link voltage fluctuations and significantly degrade power quality compensation performance. Thus, DC-link voltage control of the UPQC plays a key role in regulating the power absorbed or supplied by the DC-link capacitor, stabilizing the load voltage, and improving power quality under grid voltage distortions and sudden load changes. As a result, a Legendre Petri fuzzy neural network (LPFNN) controller is employed in place of the traditional proportional-integral (PI) and fuzzy neural network (FNN) controllers for DC-link voltage control and power quality improvement. Finally, the experimental results using the developed LPFNN-controlled UPQC are provided to verify the effectiveness of regulating DC-link voltage and improving power quality compared with the PI and FNN-controlled UPQCs under grid voltage distortions and sudden load changes. The lagging PF, current THD, CUR, and settling time of the DC-link voltage are significantly improved to 0.99, 2.9%, 2.7% and 825 ms, which are superior to the PI controller (0.98, 3.6%, 3.5% and 1220 ms) and FNN controllers (0.99, 3.2%, 3.2% and 915 ms).

Keywords: unified power quality conditioner; power quality; power sharing; intelligent control; Legendre Petri fuzzy neural network

Check for updates

Academic Editors: Pooyan Alinaghi Hosseinabadi, Mehdi Seyedmahmoudian, Evan Franklin and Waqas Hassan

Received: 30 September 2026
Revised: 28 October 2026
Accepted: 3 November 2026
Published: 5 November 2026

Copyright: © 2026 by the authors. Licensee MDPI, Basel, Switzerland. This article is an open access article distributed under the terms and conditions of the Creative Commons Attribution (CC BY) license.

1. Introduction

Recently, because of the increasing penetration of renewable energy resource-based distributed generators (DGs) and the widespread use of high-precision and sensitive equipment, such as factory automation systems, medical equipment, and semiconductor manufacturing equipment, power quality issues have attracted significant attention [1,2]. The common power quality issues can be divided into two types: voltage-related and current-related power quality issues [3]. The voltage-related power quality issues mainly result from grid voltage disturbances, such as voltage sags, swells and unbalance [4].

Abnormal grid voltages can adversely affect the reliable operation of the power system and may damage users' electrical appliances and equipment. Moreover, nonlinear, inductive, and unbalanced loads lead to current-related power quality issues, such as current total harmonic distortion (THD), lagging power factor (PF), and unbalanced grid currents, thereby reducing operating efficiency and increasing power losses [1,5].

Generally, active power filters (APFs), distribution static compensators (DSTATCOMs) and dynamic voltage restorers (DVRs) have been widely employed to mitigate power quality issues due to their relatively simple structure [6,7]. The APF and DSTATCOM can solve current-related power quality issues. On the other hand, voltage-related power quality issues can be overcome by the DVR. Nevertheless, these devices cannot simultaneously mitigate both voltage-related and current-related power quality issues. The unified power quality conditioner (UPQC) has been regarded as a comprehensive solution by connecting shunt and series inverters back-to-back to cope with both supply voltage and load current imperfections [8,9]. In other words, the shunt inverter of the UPQC can be regarded as the DSTATCOM to compensate for harmonic currents and reactive power for current THD reduction, PF correction, and grid current balancing [10,11]. Then, the series inverter of the UPQC is considered as the DVR to stabilize the load voltage when grid voltage distortions, such as voltage sags, swells, and unbalance, occur [10,11]. Consequently, much literature regarding the UPQC for power quality improvement has been reported [12–15]. A UPQC is integrated with electric vehicles, renewable energy resources and storage systems to address power quality problems [13]. In [14], a transformerless single-phase UPQC based on three-leg and standby converters is proposed to reduce waveform harmonic distortion and semiconductor losses. Moreover, a coordinated direct power control strategy for a modular multilevel converter-based UPQC is given in [15] to allocate the series-side output power and balance the power between the series and shunt sides. Though the shunt inverter of the UPQC is mainly responsible for reactive power compensation to mitigate current-related power quality issues, some studies using phase angle control for reactive power sharing have proposed that part of the load reactive power demand be supplied by the series inverter to enhance its utilization [16–18].

Because the shunt and series inverters of the UPQC are interconnected in a back-to-back configuration through a DC-link capacitor, the power mismatch between the series and shunt inverters of the UPQC can result in DC-link voltage fluctuations and significantly degrade the power quality compensation performance. Moreover, though the series inverter can also share part of the load reactive power demand by using phase angle control to enhance utilization, the power required for reactive power sharing is still exchanged through the DC-link capacitor. Thus, DC-link voltage control of the UPQC plays a key role in regulating the power absorbed or supplied by the DC-link capacitor, stabilizing the load voltage, and improving power quality under grid voltage distortions and sudden load changes [19–21]. Nevertheless, the conventional linear proportional–integral (PI) controller for DC-link voltage control of the UPQC cannot effectively cope with external disturbances, such as sudden load changes and grid voltage distortions, resulting in sluggish dynamic responses and high current THD [22,23].

In the past decades, the rapid development of artificial intelligence (AI) and machine learning (ML) has attracted considerable attention, leading to widespread applications in both industry and academia. AI and ML algorithms enable control systems to learn from data, adapt to changing operating conditions, and generate appropriate control outputs based on the learned information [24,25]. The Legendre Petri fuzzy neural network (LPFNN) controller is an ML-based intelligent controller that combines a Petri net (PN), Legendre polynomials, fuzzy logic, and neural networks (NNs) [1]. Because of the advanced characteristics and network structure, the LPFNN inherits the advantages of Legendre

polynomials in approximating nonlinear functions with high accuracy over a bounded interval [26,27]. The PN has emerged as a popular modeling language for representing concurrent and discrete processes due to its expressiveness, ability to handle concurrency and conflicts, formal representation capabilities, and compatibility with mathematical analysis [28]. Consequently, the PN is a powerful tool for modeling, analyzing, optimizing, and controlling dynamic systems. Moreover, the fuzzy logic algorithm provides an efficient method to represent and minimize the deleterious effects of uncertainties through appropriately designed fuzzy rules [29]. Furthermore, the NN possesses learning and memory capabilities by mimicking the interconnections and signal propagation of neurons in the human brain [30]. As a result, because of the above merits, the LPFNN is adopted in this study for the DC-link voltage control of the UPQC [1].

In this study, a three-phase, four-leg intelligent UPQC with reactive power sharing capability is developed to mitigate voltage and current-related power quality issues. Moreover, since the power required by the UPQC is absorbed or supplied by the DC-link capacitor, DC-link voltage control of the UPQC plays a key role in stabilizing the load voltage and improving power quality under grid voltage distortions and sudden load changes. As a result, the LPFNN is adopted for DC-link voltage control in the UPQC to improve the dynamic response of the DC-link voltage and enhance power quality under grid voltage distortions and sudden load changes. The remainder of this study is organized as follows: The control principle of the UPQC is described in Section 1. The network structure of the adopted LPFNN is represented in Section 2. The experimental results using the developed LPFNN-controlled UPQC are provided in Section 4. Then, the conclusion is given in Section 5.

2. Control Principle of UPQC

The schematic configuration of the developed UPQC with reactive power sharing capability is shown in Figure 1. The UPQC is composed of a shunt inverter and a series inverter, which are connected in a back-to-back configuration via a DC-link capacitor. The three-phase, four-leg shunt inverter is connected in parallel with multiple loads, including a linear inductive load, a nonlinear load and an unbalanced load. The main function of the shunt inverter is to compensate for harmonic currents and reactive power for current THD reduction, PF correction, and grid current balancing. Moreover, the series inverter is connected in series with the power grid via a series transformer with a turns ratio of 1:1 and is responsible for compensating for grid voltage distortions to stabilize the load voltage. The block diagram of the developed UPQC is illustrated in Figure 2. The detailed control principle of the UPQC is described as follows.

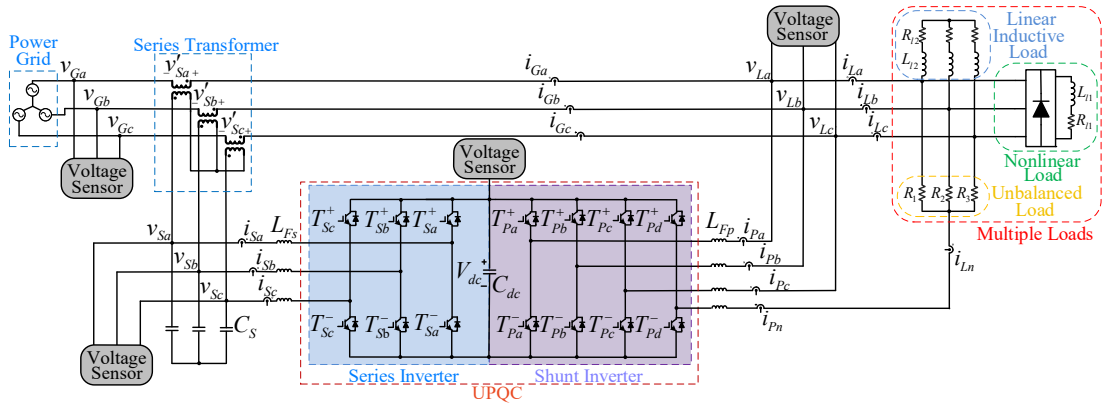


Figure 1. Schematic configuration of the developed UPQC.

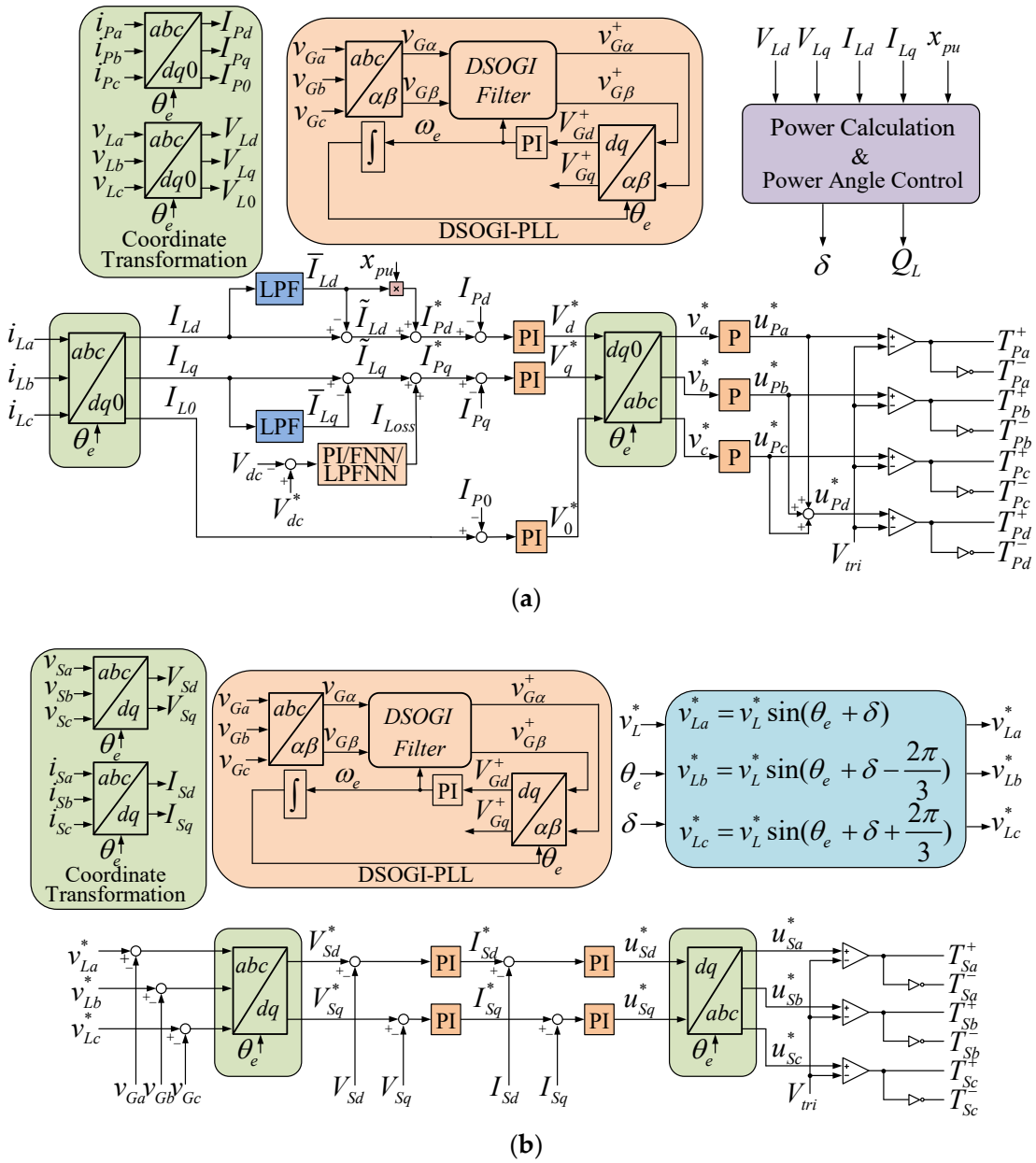


Figure 2. Block diagram of the developed UPQC: (**a**) Control block of the shunt inverter. (**b**) Control block of the series inverter.

2.1. Control Algorithm of Shunt Inverter

The control block of the shunt inverter in the UPQC is shown in Figure 2a. First, to achieve accurate synchronization with the power grid and compute the electrical angle θ_e, a dual second-order generalized integrator phase-locked loop (DSOGI-PLL) is employed in the shunt inverter of the UPQC. The detected three-phase grid voltages v_{Ga}, v_{Gb}, v_{Gc} are transformed into the $\alpha\beta$-axis grid voltages $v_{G\alpha}$, $v_{G\beta}$ through the $abc/\alpha\beta$ coordinate transformation. The $\alpha\beta$-axis positive-sequence voltages v^+_{Ga}, $v^+_{G\beta}$ are computed via the DSOGI filter and then transformed into the dq-axis positive-sequence voltage components V^+_{Gd}, V^+_{Gq} through $\alpha\beta/dq$ coordinate transformation. Subsequently, the angular frequency ω_e is computed by the PI controller using the d-axis positive-sequence voltage component V^+_{Gd} as input. Then, the electrical angle θ_e is obtained by integrating the angular frequency ω_e and is used for grid synchronization and coordinate transformation. On the other hand, the q-axis positive-sequence component V^+_{Gq} corresponds to the peak value of the

grid phase voltage. Moreover, the three-phase load voltages v_{La}, v_{Lb}, v_{Lc}, load currents i_{La}, i_{Lb}, i_{Lc} and output currents of the shunt inverter i_{Pa}, i_{Pb}, i_{Pc} are detected to compute the corresponding $dq0$-axis load voltages V_{Ld}, V_{Lq}, V_{L0}, load currents I_{Ld}, I_{Lq}, I_{L0} and output currents I_{Pd}, I_{Pq}, I_{P0} via the $abc/dq0$ coordinate transformation with the electric angle θ_e. In this study, the power angle control is adopted for the series inverter to supply part of the load reactive power demand and reduce the required VA rating of the shunt inverter [16,18]. The main objective of the power angle control is to determine the series injection angle by estimating the power angle δ. The power angle δ is adaptively computed from the instantaneous active and reactive powers of the load, which ensures fast and accurate angle estimation. Therefore, the power angle δ can be described as follows [18].

$$\delta = \sin^{-1}(n_O \cdot \frac{(V_{Lq} \cdot I_{Ld} - V_{Ld} \cdot I_{Lq}) \cdot (1 - x_{pu})}{V_{Ld} \cdot I_{Ld} + V_{Lq} \cdot I_{Lq}}); \; n_O = \frac{|v'_G|}{|v_L|} \tag{1}$$

where n_O stands for the ratio of the grid voltage after the voltage disturbance to the rated load voltage, and x_{pu} depicts the reactive power-sharing ratio of the shunt inverter. Consequently, the reactive power-sharing ratio x_{pu}, the corresponding dq-axis load voltages V_{Ld}, V_{Lq} and load currents I_{Ld}, I_{Lq} are sent to the power calculation and power angle control for computing the reactive power Q_L of the loads and the power angle δ, as shown in Figure 2a. Furthermore, the dq-axis load currents I_{Ld}, I_{Lq} generally comprise the dc current components $\bar{I}_{Ld}$, $\bar{I}_{Lq}$ and ac current components $\tilde{I}_{Ld}$, $\tilde{I}_{Lq}$. Hence, two low-pass filters (LPFs) are adopted in dq-axis load currents I_{Ld}, I_{Lq}, respectively, to extract the load dc current components $\bar{I}_{Ld}$, $\bar{I}_{Lq}$, and then subtracted from the dq-axis load currents I_{Ld}, I_{Lq} to obtain the load ac current components $\tilde{I}_{Ld}$, $\tilde{I}_{Lq}$ [1]. Subsequently, the d-axis load dc current component $\bar{I}_{Ld}$ is multiplied by the reactive power-sharing ratio x_{pu} of the shunt inverter and then is added to the d-axis load ac current component $\tilde{I}_{Ld}$ to obtain the d-axis current command I^*_{Pd}. On the other hand, to effectively improve power quality under grid voltage distortions and sudden load changes, the DC-link voltage error $V^*_{dc} - V_{dc}$ is transmitted to the traditional PI, FNN and the adopted LPFNN controllers to generate the power loss I_{Loss}. Thus, the q-axis current command I^*_{Pq} is obtained by adding the q-axis load ac current component $\tilde{I}_{Lq}$ to the power loss I_{Loss}. Afterwards, the dq-axis current commands I^*_{Pd}, I^*_{Pq} are compared with the dq-axis output currents I_{Pd}, I_{Pq}, and the resulting current errors are processed by the PI controllers to generate the dq-axis voltage commands V^*_d, V^*_q. Similarly, the 0-axis voltage command V^*_0 can be computed by using the 0-axis current error $I^*_{L0} - I_{P0}$ via the PI controller. The $dq0$-axis voltage commands V^*_d, V^*_q, V^*_0 are transformed into the three-phase voltage commands v^*_a, v^*_b, v^*_c via the $dq0/abc$ coordinate transformation. In addition, three-phase reference commands u^*_{Pa}, u^*_{Pb}, u^*_{Pc} are acquired through the P controller. Thus, to suppress the neutral load current, the four-leg reference neutral current u^*_{Pd} of the shunt inverter is computed as follows:

$$u^*_{Pd} = u^*_{Pa} + u^*_{Pb} + u^*_{Pc} \tag{2}$$

Finally, the three-phase, four-leg reference commands u^*_{Pa}, u^*_{Pb}, u^*_{Pc}, u^*_{Pd} are compared with the triangular carrier waveform V_{tri} at the switching frequency for the generation of the switching signals T^+_{Pa}, T^-_{Pa}, T^+_{Pb}, T^-_{Pb}, T^+_{Pc}, T^-_{Pc}, T^+_{Pd}, T^-_{Pd} of the shunt inverter. Therefore, the DC-link voltage fluctuation and current-related power quality issues can be mitigated by the shunt inverter.

2.2. Control Algorithm of Series Inverter

The control block of the series inverter in the UPQC is shown in Figure 2b. First, the three-phase compensation voltages v_{Sa}, v_{Sb}, v_{Sc} and output currents i_{Sa}, i_{Sb}, i_{Sc} of the series inverter are measured and transformed into the corresponding dq-axis compensation voltages V_{Sd}, V_{Sq} and output currents I_{Sd}, I_{Sq} via abc/dq coordinate transformation using

electric angle θ_e. Moreover, in this study, to enable the series inverter to supply part of the load reactive power demand, the three-phase load voltage commands v_{La}^*, v_{Lb}^*, v_{Lc}^* are derived based on the amplitude of the load voltage command v_L^*, electric angle θ_e, and power angle δ, and are expressed as follows [18]:

$$\begin{aligned} v_{La}^* &= v_L^* \sin(\theta_e + \delta) \\ v_{Lb}^* &= v_L^* \sin(\theta_e + \delta - \tfrac{2\pi}{3}) \\ v_{Lc}^* &= v_L^* \sin(\theta_e + \delta + \tfrac{2\pi}{3}) \end{aligned} \tag{3}$$

The obtained three-phase load voltage commands v_{La}^*, v_{Lb}^*, v_{Lc}^* are compared with the three-phase grid voltages v_{Ga}, v_{Gb}, v_{Gc} and the resulting voltage errors are transmitted to abc/dq coordinate transformation for obtaining the dq-axis compensation voltage commands V_{Sd}^*, V_{Sq}^*. Then, the errors between the dq-axis compensation voltage commands V_{Sd}^*, V_{Sq}^* and the actual compensation voltages V_{Sd}, V_{Sq} are sent to two PI controllers to obtain the dq-axis current commands I_{Sd}^*, I_{Sq}^*, respectively. Similarly, the dq-axis reference commands u_{Sd}^*, u_{Sq}^* can be acquired by using the errors between the dq-axis current commands I_{Sd}^*, I_{Sq}^* and the output currents I_{Sd}, I_{Sq} through the PI controllers. Consequently, the three-phase reference commands u_{Sa}^*, u_{Sb}^*, u_{Sc}^* are computed via the dq/abc coordinate transformation using the dq-axis current commands I_{Sd}^*, I_{Sq}^* as inputs. Finally, the three-phase reference commands u_{Sa}^*, u_{Sb}^*, u_{Sc}^* are compared with the triangular carrier waveform V_{tri} to generate the switching signals T_{Sa}^+, T_{Sa}^-, T_{Sb}^+, T_{Sb}^-, T_{Sc}^+, T_{Sc}^- of the series inverter. Hence, the series inverter can mitigate voltage-related power quality issues while sharing part of the load reactive power demand. Additionally, in this study, the negative-sequence compensation is not considered in the control strategy of the series inverter.

3. Intelligent LPFNN Controller

Due to its simplicity and ease of implementation, the conventional PI controller has been extensively employed in industrial applications. Nevertheless, since the fixed parameters of the PI controller cannot adapt to varying operating conditions, its control performance may deteriorate under sudden grid voltage distortions and load changes [1,21]. Thus, the intelligent LPFNN controller is employed in place of the traditional PI and FNN controllers for DC-link voltage control in the UPQC to improve the dynamic response of the DC-link voltage and enhance power quality under grid voltage distortions and sudden load changes. The network structure and online learning based on the backpropagation (BP) algorithm of the LPFNN are described as follows [1]:

3.1. Network Structure

The network structure of the adopted LPFNN controller is illustrated in Figure 3. The adopted LPFNN is constructed with six layers, including an input layer, a membership layer, a Legendre layer, a Petri layer, a rule layer, and an output layer. The detailed signal propagation through each layer of the six-layer LPFNN controller is described as follows:

1. Layer 1 (input layer):

   The input and output of each node in the input layer are expressed as follows:

$$net_i^1(N) = x_i^1(N) \tag{4}$$

$$y_i^1(N) = f_i^1(net_i^1(N)) = net_i^1(N) \quad i = 1, 2 \tag{5}$$

   where N denotes the iteration index. In this study, the inputs of the adopted LPFNN controller are the DC-link voltage error $x_1^1(N) = e = V_{dc}^* - V_{dc}$ and its derivative $x_2^1(N) = \dot{e}$ of the shunt inverter, as shown in Figure 2a.

2. Layer 2 (membership layer):

The fuzzification process in this layer is performed using Gaussian membership functions, through which the input variables are transformed into membership degrees within the range of 0 to 1, as follows:

$$net_{im}^{2}(N) = -\frac{\left(y_{i}^{1}(N) - m_{im}^{2}(N)\right)^{2}}{\left(\sigma_{im}^{2}(N)\right)^{2}} \tag{6}$$

$$y_{im}^{2}(N) = f_{im}^{2}(net_{im}^{2}(N)) = \exp(net_{im}^{2}(N)), \quad m = 1, 2, 3 \tag{7}$$

where σ_{im}^{2} and m_{im}^{2} denote the standard deviation and mean of the Gaussian functions, respectively, and y_{im}^{2} represents the output of the imth node, representing the corresponding membership degree.

3. Layer 3 (Legendre layer):

Legendre polynomials constitute a set of orthogonal polynomials that can expand the original input vector and improve the convergence rate [27]. Hence, they are employed as basis functions for functional expansion. The input vector $x = \left[x_1^1,\ x_2^1\right]$ is then mapped into an enhanced feature space as follows [27]:

$$\begin{aligned} \lambda &= \left[\lambda_1^3(N), \lambda_2^3(N), \ldots, \lambda_l^3(N)\right]^T \\ &= \left[L_0, L_1\left(x_1^1\right), L_2\left(x_1^1\right), L_3\left(x_1^1\right), L_4\left(x_1^1\right), L_1\left(x_2^1\right), L_2\left(x_2^1\right), L_3\left(x_2^1\right), L_4\left(x_2^1\right) \right]^T \end{aligned} \tag{8}$$

where λ_l^3 denotes the outputs of the Legendre expansion; λ denotes the vector obtained through the Legendre polynomial expansion; $L_n(x)$ express the Legendre polynomials, in which $-1 < x < 1$ depicts the argument of the polynomial; and n represents the order of the expansion. The Legendre polynomials can be described as:

$$L_n(x) = \frac{1}{2^n n!}\frac{d^n}{dx^n}[(x^2 - 1)^n] \tag{9}$$

The signal processing operation in the Legendre layer is expressed as follows:

$$net_l^3(N) = \sum_{l=1}^{9} w_l^3 \lambda \tag{10}$$

$$y_l^3(N) = f_l^3(net_l^3(N)) = net_l^3(N), \quad l = 1, 2, \ldots, 9 \tag{11}$$

where w_l^3 stands for the connective weights and $y_l^3(N)$ represents the output of the lth node.

4. Layer 4 (Petri layer):

A competitive mechanism is introduced in the Petri layer to determine the node to be fired and generate the corresponding token. The presence of a token at the input place enables the associated transition. Accordingly, the firing state of the transition $t_{ip}^4(N)$ is defined as follows [1]:

$$t_{ip}^{4}(N) = \begin{cases} 1, & y_{im}^{2}(N) \geq d_t \\ 0, & y_{im}^{2}(N) < d_t \end{cases}, \quad p = 1, 2, 3 \tag{12}$$

$$d_t = \frac{\alpha \exp(-\beta H)}{1 + \exp(-\beta H)} \tag{13}$$

$$H = \frac{1}{2}(x_1^1(N) + x_2^1(N)) \tag{14}$$

where d_t denotes the dynamic threshold value; positive constants α and β are set to 2 and 0.5, respectively. Afterwards, the signal propagation through the nodes in the Petri layer is described as below:

$$net_{ip}^{4}(N) = \begin{cases} y_{im}^{2}(N), & t_{ip}^{4}(N) = 1 \\ 0, & t_{ip}^{4}(N) = 0 \end{cases} \tag{15}$$

$$y_{ip}^{4}(N) = f_{ip}^{4}(net_{ip}^{4}(N)) = net_{ip}^{4}(N) \tag{16}$$

5. Layer 5 (rule layer):

In the rule layer, the input signals are multiplied to determine the corresponding rule firing strength. The input–output relationship is expressed as follows:

$$net_r^5(N) = \prod y_l^3 y_{ip}^4(N) \tag{17}$$

$$y_r^5(N) = f_r^5(net_r^5(N)), \quad r = 1, 2, \ldots, 9 \tag{18}$$

where $y_r^5(N)$ is the output of this layer.

6. Layer 6 (output layer):

The output layer performs the defuzzification process by aggregating the incoming signals through a summation operation. The resulting output is expressed as follows:

$$net_o^6(N) = \sum_{r=1}^{9} w_r^6 y_r^5(N) \tag{19}$$

$$y_o^6(N) = f_o^6(net_o^6(N)), \ o = 1 \tag{20}$$

where w_r^6 denotes the connective weights, and $y_o^6(N)$ depicts the output of the adopted LPFNN controller for the shunt inverter of the UPQC to effectively improve the dynamic response of the DC-link voltage and enhance power quality under grid voltage distortions and sudden load changes.

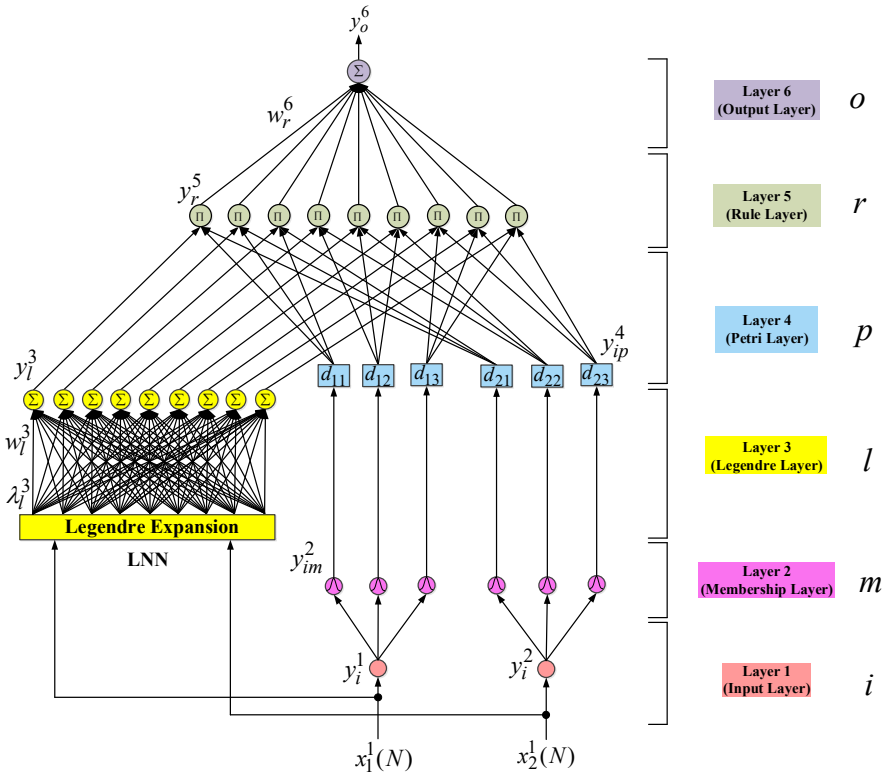


Figure 3. Network structure of the six-layer LPFNN controller.

3.2. Online Learning Based on BP Algorithm

The parameters of the adopted LPFNN for the DC-link voltage control in the shunt inverter are updated online using the BP algorithm based on a supervised learning scheme. The adjustable parameters include the connective weights and the means and standard

deviations of the membership functions. To derive the corresponding parameter update laws, the error function E is defined as follows:

$$E(N) = \frac{1}{2}\left(V_{dc}^{*} - V_{dc}\right)^2 = \frac{1}{2}e^2 \tag{21}$$

Accordingly, the online learning algorithm for the adopted LPFNN is derived in detail as follows:

1. Layer 6 (output layer):

   The propagated error term in the output layer is expressed as follows:

$$\delta_o^6 = -\frac{\partial E(N)}{\partial y_o^6(N)} = -\frac{\partial E(N)}{\partial V_{dc}}\frac{\partial V_{dc}}{\partial y_o^6(N)} \tag{22}$$

   In accordance with the chain rule, the update amount Δw_r^6 of the connective weight is derived as follows:

$$\Delta w_r^6 = -\eta_r \frac{\partial E(N)}{\partial w_r^6} = -\eta_r \left[\frac{\partial E(N)}{\partial y_o^6(N)}\right]\frac{\partial y_o^6(N)}{\partial w_r^6(N)} = \eta_r \delta_o^6 y_r^5(N) \tag{23}$$

   where η_r represents the learning rate. Hence, the connective weight w_r^6 can be updated as:

$$w_r^6(N+1) = w_r^6(N) + \Delta w_r^6 \tag{24}$$

2. Layer 5 (rule layer):

   The error terms propagated to the rule layer can be described as follows:

$$\delta_r^5 = -\frac{\partial E(N)}{\partial y_r^5(N)} = -\left[\frac{\partial E(N)}{\partial y_o^6(N)}\right]\frac{\partial y_o^6(N)}{\partial y_r^5(N)} = \delta_o^6 w_r^6(N) \tag{25}$$

3. Layer 3 (Legendre layer):

   In this layer, the term for the propagated error is expressed as follows:

$$\delta_l^3 = -\frac{\partial E(N)}{\partial y_l^3(N)} = -\left[\frac{\partial E(N)}{\partial y_o^6(N)}\frac{\partial y_o^6(N)}{\partial y_r^5(N)}\right]\frac{\partial y_r^5(N)}{\partial y_l^3(N)} = \delta_r^5 y_{1p}^4 y_{2p}^4(N) \tag{26}$$

   Then, the connective weight updates are obtained using the chain rule as follows:

$$\Delta w_l^3 = -\eta_l \frac{\partial E(N)}{\partial w_l^3(N)} = -\eta_l \left[\frac{\partial E(N)}{\partial y_o^6(N)}\frac{\partial y_o^6(N)}{\partial y_r^5(N)}\frac{\partial y_r^5(N)}{\partial y_l^3(N)}\right]\frac{\partial y_l^3(N)}{\partial w_l^3(N)} = \eta_l \delta_l^3 \lambda_l^3(N) \tag{27}$$

   where η_l stands for the learning rate. Consequently, the updated connective weight w_l^3 is acquired as follows:

$$w_l^3(N+1) = w_l^3(N) + \Delta w_l^3 \tag{28}$$

4. Layer 2 (membership layer):

   In the membership layer, the error terms can be derived as follows:

$$\delta_{im}^2 = -\frac{\partial E(N)}{\partial net_{im}^2(N)} = -\left[\frac{\partial E(N)}{\partial y_o^6(N)}\frac{\partial y_o^6(N)}{\partial y_r^5(N)}\right]\frac{\partial y_r^5(N)}{\partial y_{ip}^4(N)}\frac{\partial y_{ip}^4(N)}{\partial y_{im}^2(N)}\frac{\partial y_{im}^2(N)}{\partial net_{im}^2(N)} = \sum \delta_r^5 y_r^5(N) \tag{29}$$

   Afterwards, the updates of the mean Δm_{im}^2 and standard deviation $\Delta\sigma_{im}^2$ of the membership functions are derived as follows:

$$\begin{aligned}\Delta m_{im}^2 &= -\eta_m \frac{\partial E(N)}{\partial m_{im}^2(N)} \\ &= -\eta_m \left[\frac{\partial E(N)}{\partial y_o^6(N)}\frac{\partial y_0^6(N)}{\partial y_{im}^2(N)}\frac{\partial y_{im}^2(N)}{\partial net_{im}^2(N)}\right]\frac{\partial net_{im}^2(N)}{\partial m_{im}^2(N)} = \eta_m \delta_{im}^2 \frac{2(y_i^1(N) - m_{im}^2(N))}{\left(\sigma_{im}^2(N)\right)^2}\end{aligned} \tag{30}$$

$$\begin{aligned}\Delta\sigma_{im}^{2} &= -\eta_{\sigma}\frac{\partial E(N)}{\partial\sigma_{im}^{2}(N)}\\ &= -\eta_{\sigma}\left[\frac{\partial E(N)}{\partial y_{o}^{6}(N)}\frac{\partial y_{0}^{6}(N)}{\partial y_{im}^{2}(N)}\frac{\partial y_{im}^{2}(N)}{\partial net_{im}^{2}(N)}\right]\frac{\partial net_{ij}^{2}(N)}{\partial\sigma_{ij}^{2}(N)} = \eta_{\sigma}\delta_{im}^{2}\frac{2(y_{i}^{1}(N)-m_{im}^{2}(N))^{2}}{(\sigma_{im}^{2}(N))^{3}}\end{aligned} \tag{31}$$

where η_m and η_σ represent the learning rates. Accordingly, the mean m_{im}^2 and standard deviation σ_{im}^2 of the membership functions can be updated as follows:

$$m_{im}^{2}(N+1) = m_{im}^{2}(N) + \Delta m_{im}^{2} \tag{32}$$

$$\sigma_{im}^{2}(N+1) = \sigma_{im}^{2}(N) + \Delta\sigma_{im}^{2} \tag{33}$$

Because of uncertainties in the dynamic UPQC, such as parameter variations and external disturbances, the Jacobian $\partial V_{dc}/\partial y_o^6(N)$ of the UPQC cannot be accurately determined. To address this issue and accelerate the online adaptation of the network parameters, the delta adaptation law is adopted as follows [21]:

$$\delta_{o}^{6} \cong (V_{dc}^{*} - V_{dc}) + (\dot{V}_{dc}^{*} - \dot{V}_{dc}) = e + \dot{e} \tag{34}$$

3.3. Convergence Analysis

The choice of the learning rates for the adopted LPFNN has a momentous effect on the performance of the network. For the purpose of training the adopted LPFNN effectively, the varied learning rates [31,32], which ensure the convergence of the adopted LPFNN for DC-link voltage control, as shown in Figure 2a, are derived in this study based on the analysis of a discrete-type Lyapunov function to guarantee the boundedness of the adopted LPFNN. To guarantee the convergence of the adopted LPFNN for DC-link voltage control, specific learning rate coefficients for training the network parameters are obtained from the following convergence analysis.

The error function shown in (21) is considered a discrete-type Lyapunov function. Then, the variation of the Lyapunov function is described as follows:

$$\Delta E(N) = E(N+1) - E(N) \tag{35}$$

The linearized model [32] of the Lyapunov function is obtained via (23), (27), (30) and (31) as follows:

$$\begin{aligned}E(N+1) &= E(N) + \Delta E(N)\\ &\approx E(N) + \sum_{o=1}^{9}\left[\frac{\partial E(N)}{\partial w_{r}^{6}(N)}\Delta w_{r}^{6}\right] + \sum_{l=1}^{9}\left[\frac{\partial E(N)}{\partial w_{l}^{3}(N)}\Delta w_{l}^{3}\right] + \sum_{i=1}^{2}\sum_{m=1}^{3}\left[\frac{\partial E(N)}{\partial m_{im}^{2}(N)}\Delta m_{im}^{2} + \frac{\partial E(N)}{\partial\sigma_{im}^{2}(N)}\Delta\sigma_{im}^{2}\right]\\ &= \frac{1}{4}E(N) - \eta_{r}\sum_{r=1}^{9}\left[\frac{\partial E(N)}{\partial y_{o}^{6}(N)}\frac{\partial y_{o}^{6}(N)}{\partial w_{r}^{6}(N)}\right]^{2}\\ &+\frac{1}{4}E(N) - \eta_{l}\sum_{l=1}^{9}\left[\frac{\partial E(N)}{\partial y_{o}^{6}(N)}\frac{\partial y_{o}^{6}(N)}{\partial y_{r}^{5}(N)}\frac{\partial y_{r}^{5}(N)}{\partial y_{l}^{3}(N)}\frac{\partial y_{l}^{3}(N)}{\partial w_{l}^{3}(N)}\right]^{2}\\ &+\frac{1}{4}E(N) - \eta_{m}\sum_{i=1}^{2}\sum_{m=1}^{3}\left[\frac{\partial E(N)}{\partial y_{o}^{6}(N)}\frac{\partial y_{o}^{6}(N)}{\partial y_{r}^{5}(N)}\frac{\partial y_{r}^{5}(N)}{\partial y_{im}^{2}(N)}\frac{\partial y_{im}^{2}(N)}{\partial net_{im}^{2}(N)}\frac{\partial net_{im}^{2}(N)}{\partial m_{im}^{2}(N)}\right]^{2}\\ &+\frac{1}{4}E(N) - \eta_{\sigma}\sum_{i=1}^{2}\sum_{m=1}^{3}\left[\frac{\partial E(N)}{\partial y_{o}^{6}(N)}\frac{\partial y_{o}^{6}(N)}{\partial y_{r}^{5}(N)}\frac{\partial y_{r}^{5}(N)}{\partial y_{im}^{2}(N)}\frac{\partial y_{im}^{2}(N)}{\partial net_{im}^{2}(N)}\frac{\partial net_{im}^{2}(N)}{\partial\sigma_{im}^{2}(N)}\right]^{2}\end{aligned} \tag{36}$$

where Δw_r^6, Δw_l^3, Δm_{im}^2, and $\Delta\sigma_{im}^2$ depict the variations of the connective weights, the means and the standard deviations. If the learning rate coefficients of the adopted LPFNN are designed as:

$$\eta_{r} = \frac{E(N)}{4\left[\sum_{r=1}^{9}\left[\frac{\partial E(N)}{\partial y_{o}^{6}(N)}\frac{\partial y_{o}^{6}(N)}{\partial w_{r}^{6}(N)}\right]^{2} + \varepsilon\right]} \tag{37}$$

$$\eta_l = \frac{E(N)}{4\left[\sum_{l=1}^{9}\left[\frac{\partial E(N)}{\partial y_o^6(N)}\frac{\partial y_o^6(N)}{\partial y_r^5(N)}\frac{\partial y_r^5(N)}{\partial y_l^3(N)}\frac{\partial y_l^3(N)}{\partial w_l^3(N)}\right]^2+\varepsilon\right]} \tag{38}$$

$$\eta_m = \frac{E(N)}{4\left[\sum_{i=1}^{2}\sum_{m=1}^{3}\left[\frac{\partial E(N)}{\partial y_o^6(N)}\frac{\partial y_o^6(N)}{\partial y_r^5(N)}\frac{\partial y_r^5(N)}{\partial y_{ip}^4(N)}\frac{\partial y_{ip}^4(N)}{\partial y_{im}^2(N)}\frac{\partial y_{im}^2(N)}{\partial net_{im}^2(N)}\frac{\partial net_{im}^2(N)}{\partial m_{im}^2(N)}\right]^2+\varepsilon\right]} \tag{39}$$

$$\eta_\sigma = \frac{E(N)}{4\left[\sum_{i=1}^{2}\sum_{m=1}^{3}\left[\frac{\partial E(N)}{\partial y_o^6(N)}\frac{\partial y_o^6(N)}{\partial y_l^5(N)}\frac{\partial y_l^5(N)}{\partial y_{ip}^4(N)}\frac{\partial y_{ip}^4(N)}{\partial y_{im}^2(N)}\frac{\partial y_{im}^2(N)}{\partial net_{im}^2(N)}\frac{\partial net_{im}^2(N)}{\partial \sigma_{im}^2(N)}\right]^2+\varepsilon\right]} \tag{40}$$

and ε is a positive constant, (36) can be reformulated as follows:

$$\begin{aligned}
&E(N+1) \approx \varepsilon(\eta_r+\eta_l+\eta_m+\eta_\sigma)\\
&\approx \frac{E(N)\varepsilon}{4\left[\sum_{r=1}^{9}\left[\frac{\partial E(N)}{\partial y_o^6(N)}\frac{\partial y_o^6(N)}{\partial w_r^6(N)}\right]^2+\varepsilon\right]} + \frac{E(N)\varepsilon}{4\left[\sum_{l=1}^{9}\left[\frac{\partial E(N)}{\partial y_o^6(N)}\frac{\partial y_o^6(N)}{\partial y_r^5(N)}\frac{\partial y_r^5(N)}{\partial y_l^3(N)}\frac{\partial y_l^3(N)}{\partial w_l^3(N)}\right]^2+\varepsilon\right]}\\
&+\frac{E(N)\varepsilon}{4\left[\sum_{i=1}^{2}\sum_{m=1}^{3}\left[\frac{\partial E(N)}{\partial y_o^6(N)}\frac{\partial y_o^6(N)}{\partial y_r^5(N)}\frac{\partial y_r^5(N)}{\partial y_{ip}^4(N)}\frac{\partial y_{ip}^4(N)}{\partial y_{im}^2(N)}\frac{\partial y_{im}^2(N)}{\partial net_{im}^2(N)}\frac{\partial net_{im}^2(N)}{\partial m_{im}^2(N)}\right]^2+\varepsilon\right]}\\
&+\frac{E(N)\varepsilon}{4\left[\sum_{i=1}^{2}\sum_{m=1}^{3}\left[\frac{\partial E(N)}{\partial y_o^6(N)}\frac{\partial y_o^6(N)}{\partial y_l^5(N)}\frac{\partial y_l^5(N)}{\partial y_{ip}^4(N)}\frac{\partial y_{ip}^4(N)}{\partial y_{im}^2(N)}\frac{\partial y_{im}^2(N)}{\partial net_{im}^2(N)}\frac{\partial net_{im}^2(N)}{\partial \sigma_{im}^2(N)}\right]^2+\varepsilon\right]}\\
&\le \frac{E(N)}{4}+\frac{E(N)}{4}+\frac{E(N)}{4}+\frac{E(N)}{4} = E(N)
\end{aligned} \tag{41}$$

Finally, the convergence of the adopted LPFNN control for DC-link voltage control is guaranteed according to (21) and (41). Therefore, the convergence of the DC-link voltage control of the UPQC can be ensured.

4. Experimental Results and Validation

To mitigate the voltage- and current-related power quality issues, the three-phase, four-leg intelligent UPQC with reactive power sharing capability is developed in this study. Moreover, the LPFNN is adopted for DC-link voltage control of the UPQC to effectively stabilize the load voltage and improve power quality under grid voltage distortions and sudden load changes. The experimental setup of the developed UPQC is shown in Figure 4. The block diagrams of the shunt and series inverters are illustrated in Figures 4a and 4b, respectively. The UPQC is implemented using two TMS320F28335 (Texas Instruments, Dallas, Texas, USA) DSP-based control platforms, which are employed to control the shunt and series inverters, respectively. Both platforms operate with a sampling time of 1 ms and a switching frequency of 16 kHz. The inner current-control loop and the outer voltage-control loop, incorporating the LPFNN controller in the developed UPQC control platforms, operate at frequencies of 1 kHz and 16 kHz, respectively. Furthermore, KIKUSUI PCR2000LE (KIKUSUI, Yokohama, Japan) programmable AC power supplies are employed to emulate abnormal grid voltage conditions. The nominal grid voltage and frequency for the experimental tests are set to 110 Vrms and 60 Hz, respectively. The photograph of the experimental setup is shown in Figure 4c. Afterwards, the detailed parameter setup and specifications of the developed UPQC are given in Table 1. In this study, the three-phase current unbalance ratio (CUR) and voltage unbalance ratio (VUR) are adopted as performance indices to

evaluate the current and voltage compensation performance of the developed UPQC and are defined as follows [33].

$$\text{CUR} = \frac{\text{Max}(i_{Ga}, i_{Gb}, i_{Gc}) - \text{Min}(i_{Ga}, i_{Gb}, i_{Gc})}{\text{Average}(i_{Ga}, i_{Gb}, i_{Gc})} 100\ \% \tag{42}$$

$$\text{VUR} = \frac{\text{Max}((v_{Lab}, v_{Lbc}, v_{Lca}) - \text{Average}(v_{Lab}, v_{Lbc}, v_{Lca}))}{\text{Average}(v_{Lab},\ v_{Lbc},\ v_{Lca})} 100\% \tag{43}$$

where $\text{Average}(i_{Ga}, i_{Gb}, i_{Gc})$ and $\text{Average}(v_{Lab}, v_{Lbc}, v_{Lca})$ depict the average RMS current of the grid currents i_{Ga}, i_{Gb}, i_{Gc} and the average peak value of the line-to-line load voltages $v_{Lab}, v_{Lbc}, v_{Lca}$; $\text{Max}(i_{Ga}, i_{Gb}, i_{Gc})$ and $\text{Min}(i_{Ga}, i_{Gb}, i_{Gc})$ denote the maximum and minimum RMS currents of the grid currents i_{Ga}, i_{Gb}, i_{Gc}, respectively; $\text{Max}((v_{Lab},\ v_{Lbc},\ v_{Lca}) - \text{Avg}(v_{Lab},\ v_{Lbc},\ v_{Lca}))$ expresses the maximum error between the peak values of the line-to-line load voltages $v_{Lab}, v_{Lbc}, v_{Lca}$ and the average peak value of the load voltages $v_{Lab}, v_{Lbc}, v_{Lca}$. The VUR is adopted as a performance index based on IEEE Std. 1159-2019 regulation [33]. According to the referenced standard, VUR should remain below 5% to ensure acceptable power quality. Therefore, lower CUR and VUR values correspond to improved current and voltage compensation performance of the UPQC.

Table 1. Parameters setup and specifications of the developed UPQC.

Parameters	Values
DC-Link Capacitor C	8000 μF
DC-Link Voltage V_{dc}	240 V
Filter Inductor of Series Inverter L_{Fs}	10 mH
Filter Capacitor of Series Inverter C_S	45.48 μF
Filter Inductor of Shunt Inverter L_{Fp}	3 mH
Turns Ratio of Series Transformer	1:1
Rated Power of Series Transformer	9 kVA
Sampling Frequency of UPQC	1 kHz
Switching Frequency of UPQC	16 kHz
Nominal Grid Voltage	110 Vrms
Nominal Grid Frequency	60 Hz

In this study, to verify the effectiveness of the LPFNN-controlled UPQC, two test cases are designed as follows: In case 1, the loads comprise the nonlinear load $L_{l1} = 1$ mH, $R_{l1} = 75\ \Omega$ and linear inductive load $R_{l2} = 25\ \Omega$, $L_{l2} = 30$ mH. Meanwhile, an unbalanced grid condition is introduced at 10 s, with voltage sags of 15%, 20%, and 25% applied to v_{Ga}, v_{Gb} and v_{Gc}, respectively. The reactive power-sharing ratio x_{pu} of the shunt inverter is set to 0.4, which indicates that the shunt and series inverters supply 40% and 60% of the load reactive power demand, respectively. In case 2, the loads are composed of the nonlinear load $L_{l1} = 1$ mH, $R_{l1} = 75\ \Omega$, unbalanced load $R_1 = 80\ \Omega$, $R_2 = 40\ \Omega$, $R_3 = 96\ \Omega$ and linear inductive load $R_{l2} = 25\ \Omega$, $L_{l2} = 30$ mH. Then, the linear inductive load is changed from $R_{l2} = 25\ \Omega$, $L_{l2} = 30$ mH to $R_{l2} = 25\ \Omega$, $L_{l2} = 50$ mH at 4 s. Meanwhile, a three-phase grid voltage sag of 20% is introduced at 10 s, and the grid voltage recovers to its nominal value at 16 s. In this case, the reactive power-sharing ratio x_{pu} of the shunt inverter is set to 0.5, indicating that the shunt and series inverters each supply 50% of the load reactive power demand. Moreover, to compare the compensation performance of the adopted LPFNN-controlled UPQC, the experimental results of the traditional PI- and FNN-controlled UPQCs for DC-link voltage control and power quality improvement are also provided. In this study, the gains of the PI controller for DC-link voltage control are obtained by trial and error in order to achieve good transient and steady-state control performance at different operating conditions of the UPQC. In case 1, the resulted gains are $K_P = 1$ and $K_I = 1.5$. The resulting gains $K_P = 2$, $K_I = 0.01$ are adopted in case 2.

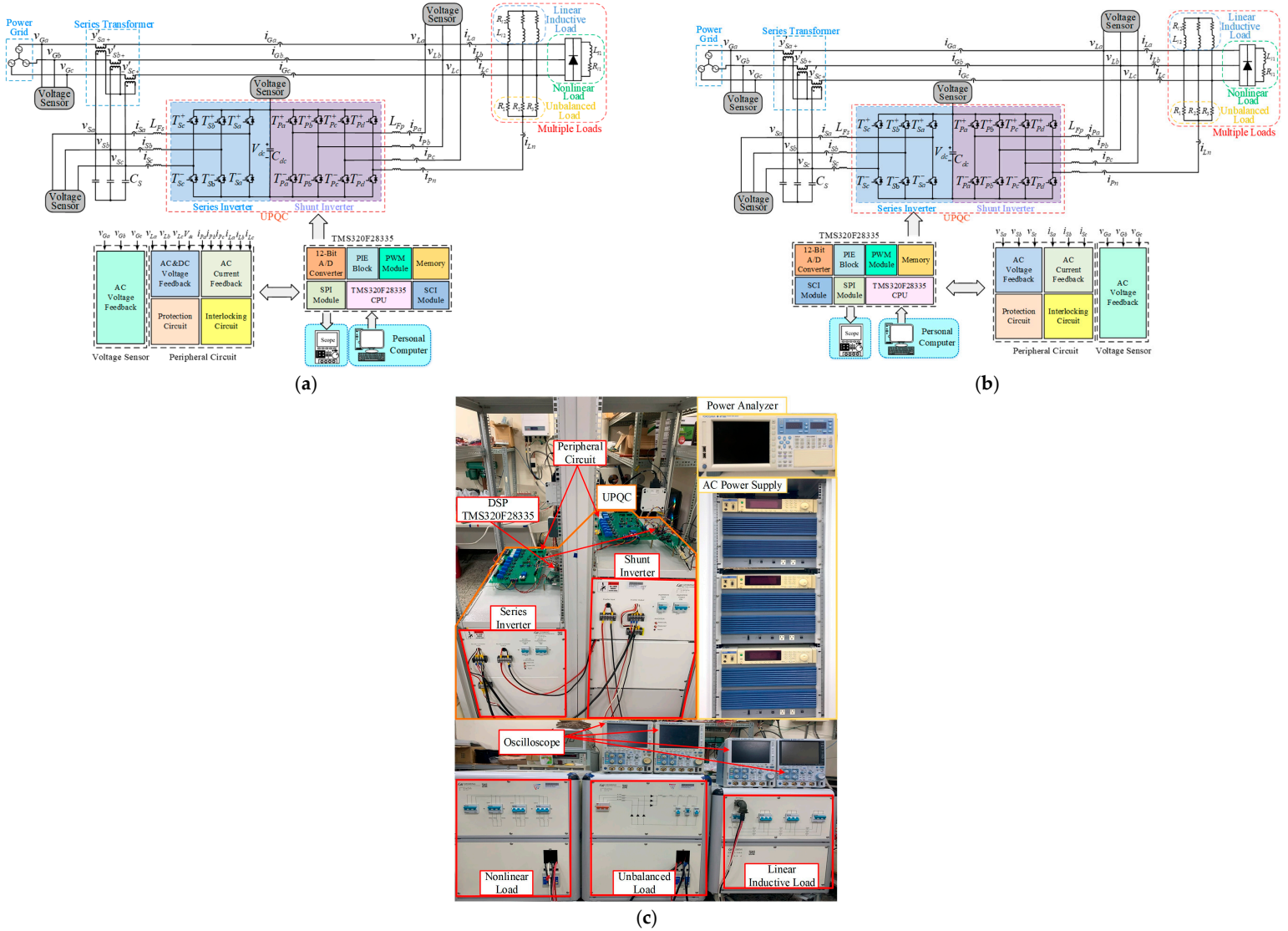


Figure 4. Experimental setup of the developed UPQC: (**a**) Block diagram of the shunt inverter. (**b**) Block diagram of the series inverter. (**c**) Photograph of the experimental setup.

https://doi.org/10.3390/en19215315

First, the experimental result without using the developed UPQC in case 1 is represented in Figure 5. The responses of the grid voltage v_G, compensation voltage v'_S of the series transformer and load voltage v_L are given in Figure 5a. The responses of the grid voltage v_{Ga}, grid current i_{Ga}, output current i_{Pa} of the shunt inverter and load current i_{La} are provided in Figure 5b. The responses of the grid voltage v_G, compensation voltage v'_S of the series transformer and load voltage v_L in the interval 9.8–10.2 s are illustrated in Figure 5c. The responses of the grid voltage v_{Ga}, grid current i_{Ga}, output current i_{Pa} of the shunt inverter and load current i_{La} in the interval 9.8–10.2 s are shown in Figure 5d. The responses of the power angle δ, load reactive power Q_L, reactive power Q_S of the series inverter, and reactive power Q_P of the shunt inverter are represented in Figure 5e. From the experimental results shown in Figure 5a,c, in the absence of the UPQC, when the unbalanced grid condition is introduced at 10 s, the load voltage v_L becomes unbalanced, resulting in a significant voltage-related power quality issue with a VUR of 6.55%. Moreover, because of the nonlinear load and linear inductive load, the current-related power quality issues are significant, with a current THD of 9.6% and a lagging PF of 0.94, as shown in Figure 5d. The load reactive power Q_L is 251 Var before 10 s and 160 Var after 10 s, as shown in Figure 5e. Furthermore, the experimental result of the PI-controlled UPQC in case 1 is provided in Figure 6. The responses of the grid voltage v_G, compensation voltage v'_S of the series transformer and load voltage v_L are given in Figure 6a. The responses of the grid voltage v_{Ga}, grid current i_{Ga}, output current i_{Pa} of the shunt inverter and load current i_{La} are provided in Figure 6b. The responses of the grid voltage v_G, compensation voltage v'_S of the series transformer and load voltage v_L in the interval 9.8–10.2 s are illustrated in Figure 6c. The responses of the grid voltage v_{Ga}, grid current i_{Ga}, output current i_{Pa} of the shunt inverter and load current i_{La} in the interval 9.8–10.2 s are shown in Figure 6d. The responses of the power angle δ, load reactive power Q_L, reactive power Q_S of the series inverter, and reactive power Q_P of the shunt inverter are represented in Figure 6e. The response of the DC-link voltage is provided in Figure 6f. In accordance with the experimental results, owing to the use of the developed UPQC, when the unbalanced grid condition is introduced at 10 s, the series inverter of the UPQC compensates for the grid voltage unbalance to maintain the load voltage at the nominal voltage level, as shown in Figure 6a,c. The VUR of the load voltage is reduced to 3.1%. As shown in Figure 6d, owing to the compensation provided by the shunt inverter of the UPQC, the current THD and lagging PF are also improved to 3.4% and 0.98, respectively. Consequently, the voltage and current-related power quality issues can be mitigated by the developed UPQC. In addition, the shunt and series inverters supply 103 Var and 155 Var of the load reactive power demand before 10 s, respectively, and 103 Var and 156 Var after 10 s, as shown in Figure 6e. The reactive power sharing capability of the developed UPQC is also verified. Nevertheless, because the fixed parameters of the PI controller for the DC-link voltage control are designed based on predefined operating conditions, the control performance may deteriorate when the UPQC is subjected to external disturbances, such as sudden grid voltage sags. Hence, when the unbalanced grid condition occurs at 10 s, the fluctuation in the DC-link voltage is obvious and the settling time Δt is 1124 ms, as shown in Figure 6f, which may degrade the power quality compensation performance. In addition, the experimental result of the FNN-controlled UPQC in case 1 is shown in Figure 7. From the experimental results, as shown in Figure 7c,d, the VUR of the load voltage is reduced to 2.9%. Then, the current THD and lagging PF are also improved to 3.1% and 0.99, respectively. The shunt and series inverters supply 40% and 60% of the load reactive power demand, respectively, as shown in Figure 7e. Afterwards, when the unbalanced grid condition occurs at 10 s, the fluctuation in the DC-link voltage is suppressed and the settling time Δt is shortened to 962 ms, as shown in Figure 7f. Additionally, the experimental result of the adopted LPFNN-controlled UPQC in case 1 is illustrated in Figure 8. Owing to the merits of

the adopted LPFNN controller, such as online learning and memory capabilities, nonlinear function approximation capability, and capabilities for modeling, analyzing, optimizing, and controlling dynamic systems, the voltage and current-related power quality issues can be effectively improved. The VUR of the load voltage is significantly reduced to 2.8%. Then, the current THD and lagging PF are also improved to 2.9% and 0.99, respectively, as shown in Figure 8c,d. The fluctuation in the DC-link voltage is also significantly suppressed at 10 s, and the settling time Δt is further shortened to 882 ms, as shown in Figure 8f. Moreover, the PF, current THD, VUR of the load, and the settling time and error of the DC-link voltage using different controllers for the UPQC after 10 s in case 1 are given in Table 2. According to the experimental results, as shown in Figures 5–8 and Table 2, the power quality issues can be solved by the developed UPQC. The reactive power-sharing ability of the series inverter is also verified. On the other hand, because of the robust control and powerful computational capabilities of the adopted LPFNN controller, the power quality issues can be effectively mitigated by using the LPFNN-controlled UPQC. When the unbalanced grid condition occurs, the fluctuation in the DC-link voltage is significantly suppressed and the settling time Δt is further shortened compared with the PI- and FNN-controlled UPQCs.

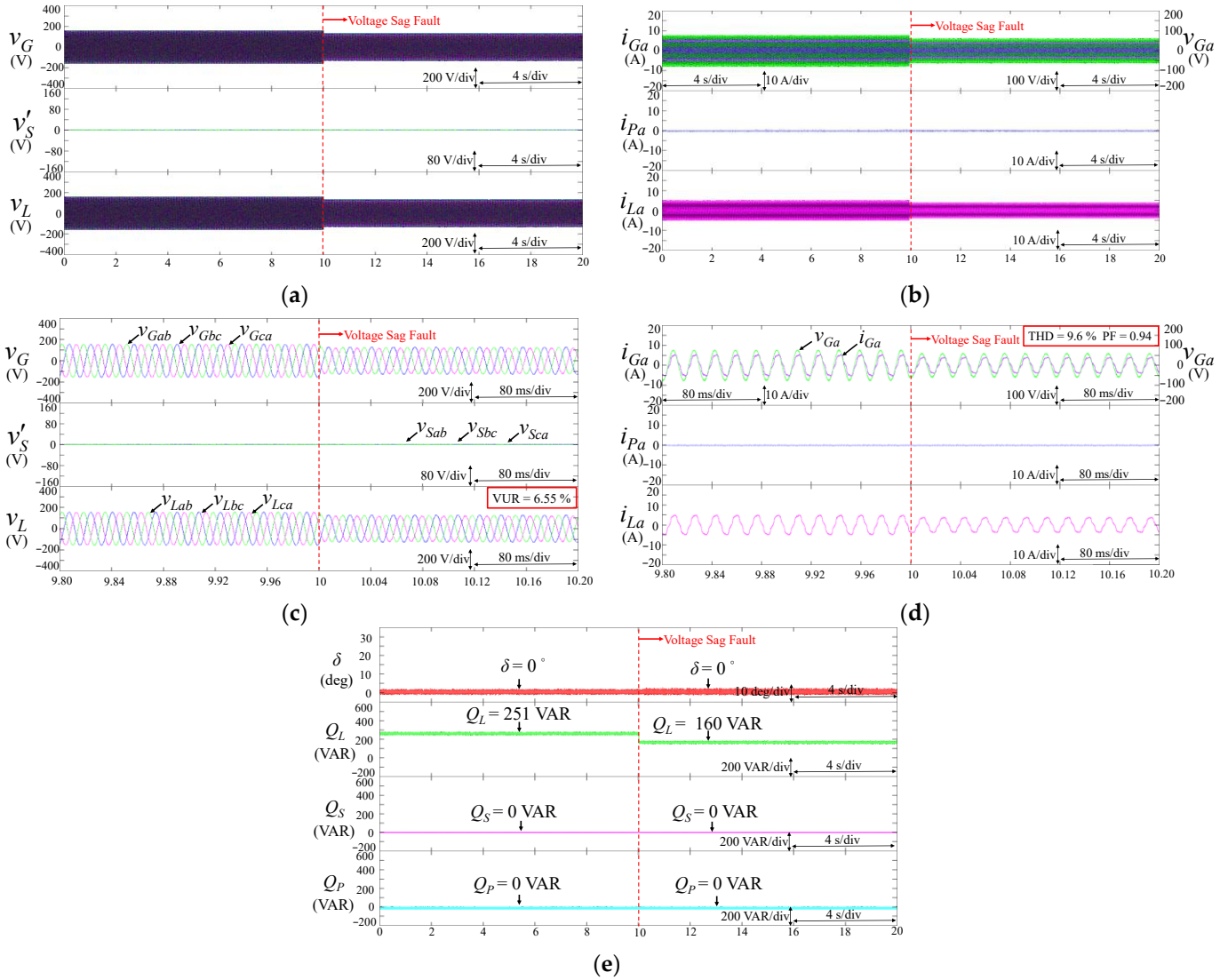


Figure 5. Experimental results without developed UPQC in case 1: (**a**) Responses of grid voltage v_G, compensation voltage v'_S of series transformer and load voltage v_L. (**b**) Responses of grid voltage v_{Ga}, grid current i_{Ga}, output current i_{Pa} of shunt inverter and load current i_{La}. (**c**) Responses of grid

voltage v_G, compensation voltage v'_S of series transformer and load voltage v_L in the interval 9.8–10.2 s. (**d**) Responses of grid voltage v_{Ga}, grid current i_{Ga}, output current i_{Pa} of shunt inverter and load current i_{La} in the interval 9.8–10.2 s. (**e**) Responses of power angle δ, load reactive power Q_L, reactive power Q_S of series inverter, and reactive power Q_P of shunt inverter.

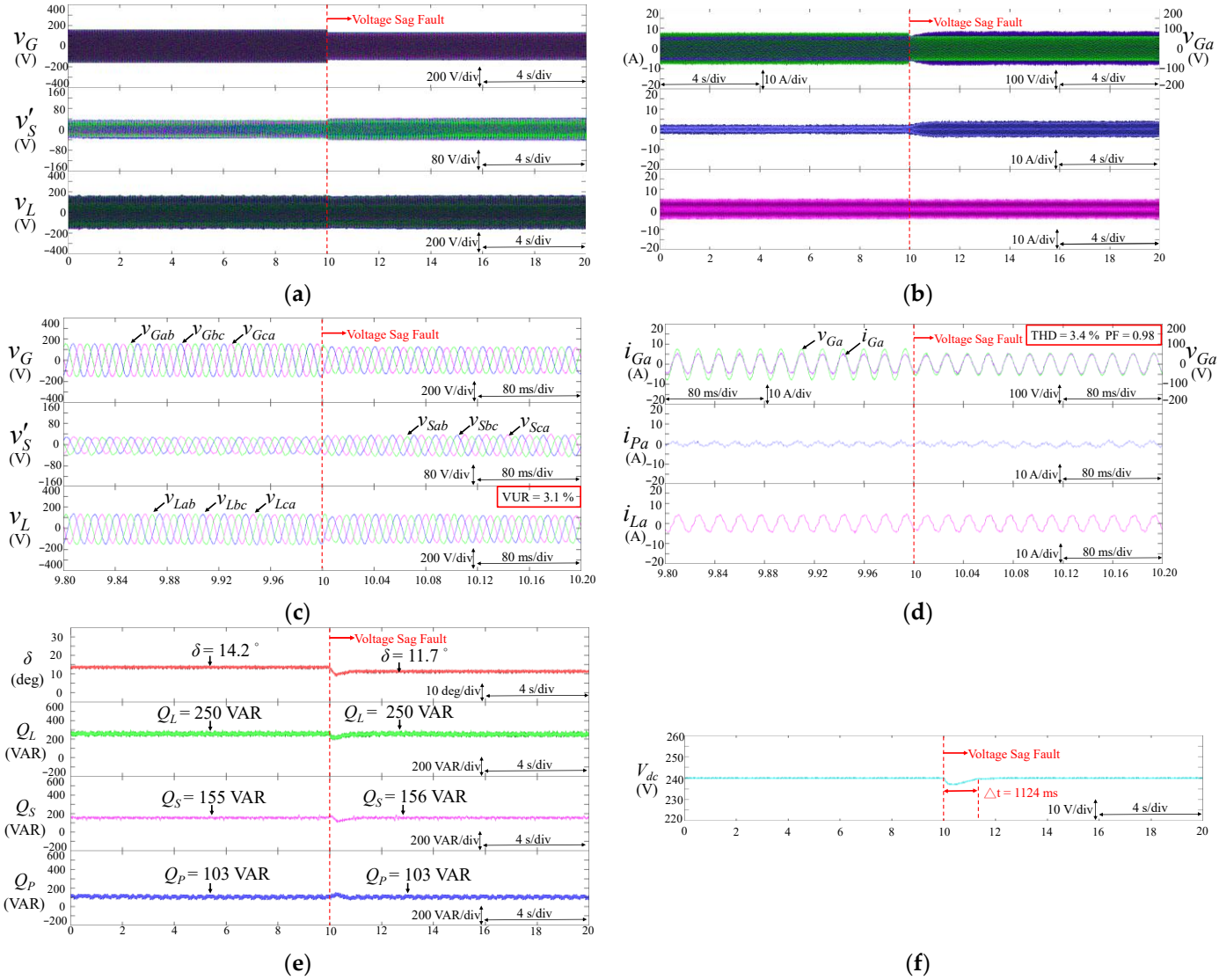


Figure 6. Experimental results of PI-controlled UPQC in case 1: (**a**) Responses of grid voltage v_G, compensation voltage v'_S of series transformer and load voltage v_L. (**b**) Responses of grid voltage v_{Ga}, grid current i_{Ga}, output current i_{Pa} of shunt inverter and load current i_{La}. (**c**) Responses of grid voltage v_G, compensation voltage v'_S of series transformer and load voltage v_L in the interval 9.8–10.2 s. (**d**) Responses of grid voltage v_{Ga}, grid current i_{Ga}, output current i_{Pa} of shunt inverter and load current i_{La} in the interval 9.8–10.2 s. (**e**) Responses of power angle δ, load reactive power Q_L, reactive power Q_S of series inverter, and reactive power Q_P of shunt inverter. (**f**) Response of DC-link voltage.

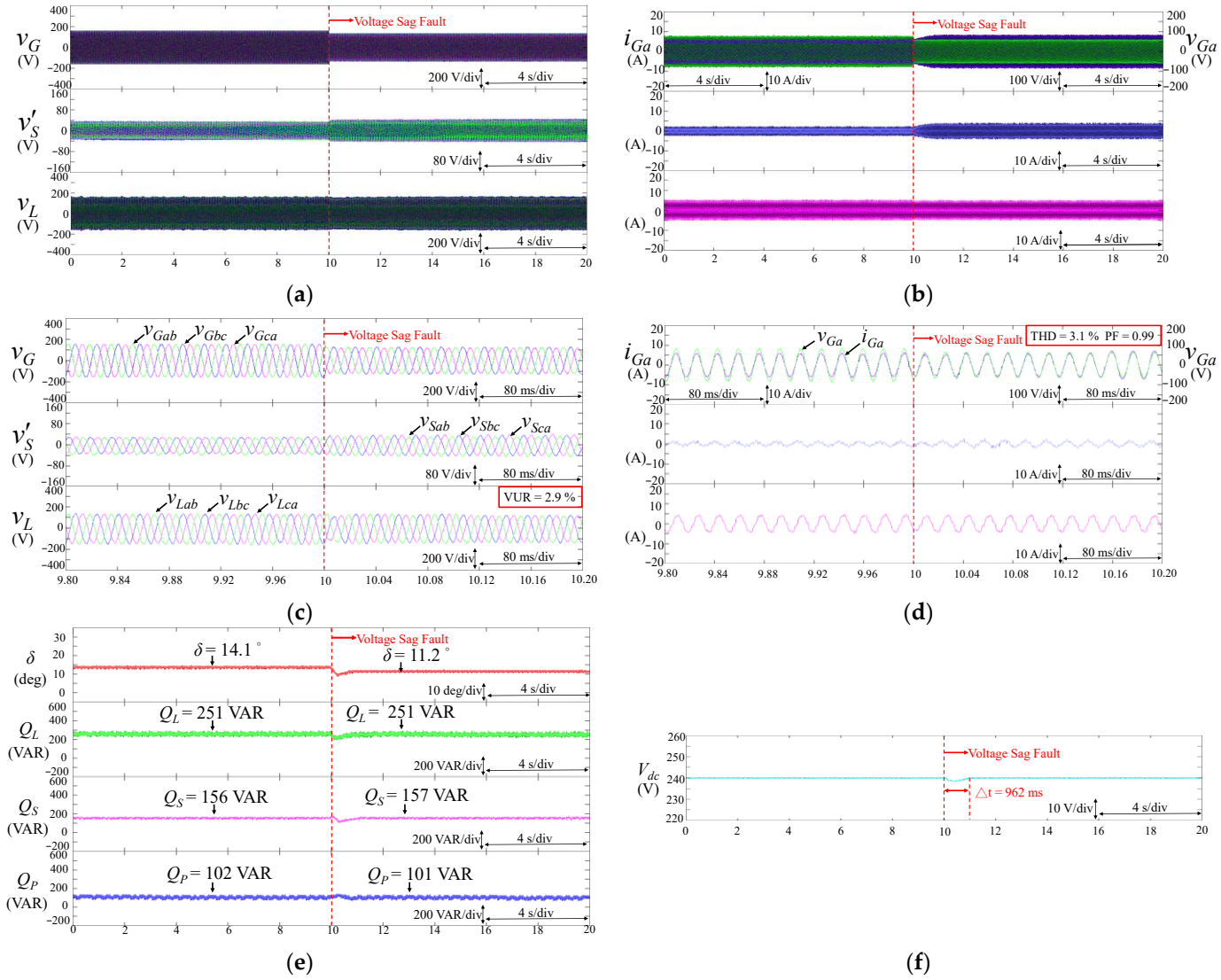


Figure 7. Experimental results of FNN-controlled UPQC in case 1: (**a**) Responses of grid voltage v_G, compensation voltage v'_S of series transformer and load voltage v_L. (**b**) Responses of grid voltage v_{Ga}, grid current i_{Ga}, output current i_{Pa} of shunt inverter and load current i_{La}. (**c**) Responses of grid voltage v_G, compensation voltage v'_S of series transformer and load voltage v_L in the interval 9.8–10.2 s. (**d**) Responses of grid voltage v_{Ga}, grid current i_{Ga}, output current i_{Pa} of shunt inverter and load current i_{La} in the interval 9.8–10.2 s. (**e**) Responses of power angle δ, load reactive power Q_L, reactive power Q_S of series inverter, and reactive power Q_P of shunt inverter. (**f**) Response of DC-link voltage.

Table 2. PF, current THD, VUR of load, and settling time and error of DC-link voltage using different controllers for UPQC after 10 s in case 1.

Case Conditions	UPQC Controllers	PF	Current THD	VUR of Load	DC-Link Voltage	
					Settling Time	Error
Case 1	None	0.94	9.6 %	6.55 %	None	None
	PI	0.98	3.4 %	3.1 %	1124 ms	3.2 V
	FNN	0.99	3.1 %	2.9 %	962 ms	2.2 V
	LPFNN	0.99	2.9 %	2.8 %	882 ms	2.0 V

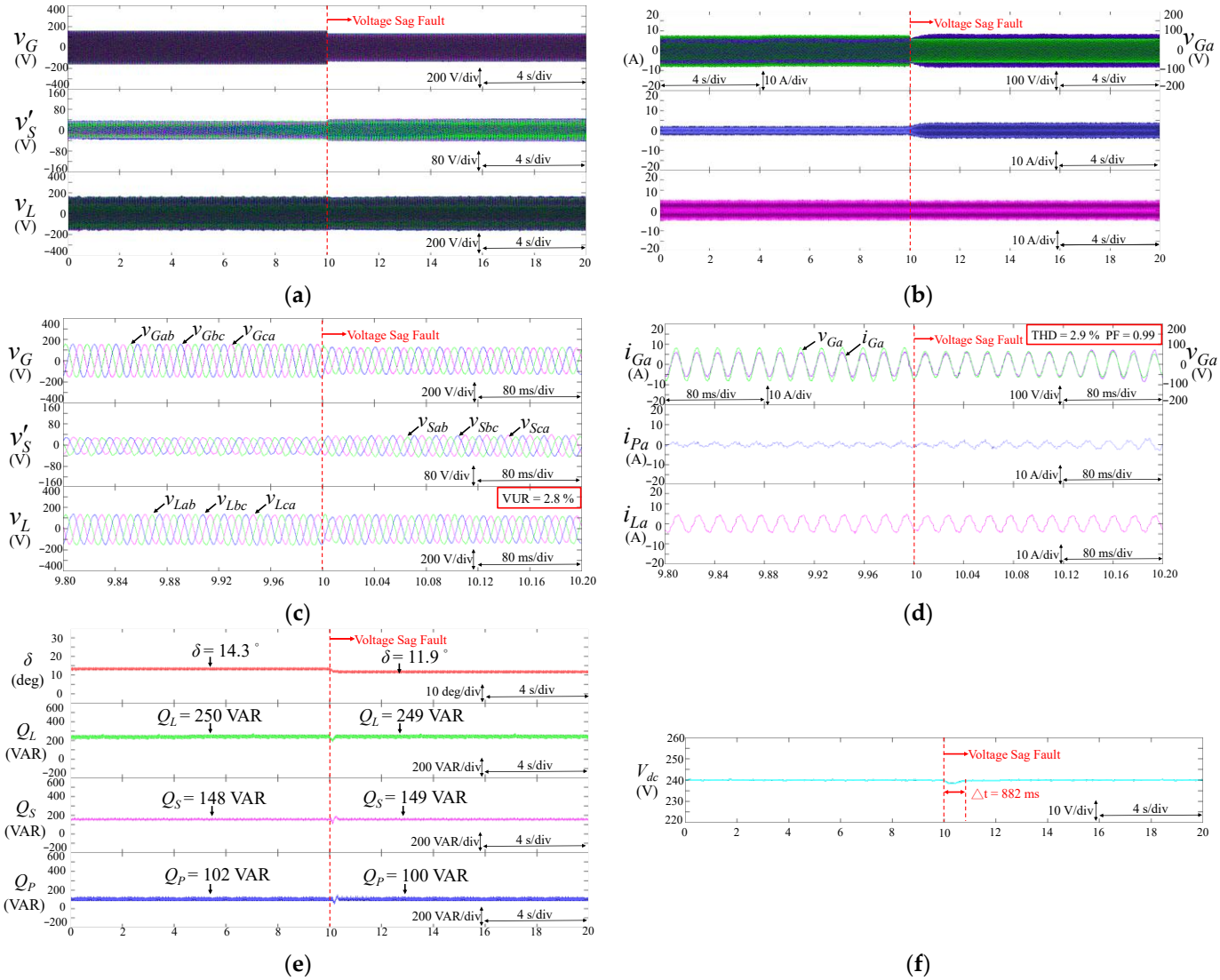


Figure 8. Experimental results of adopted LPFNN-controlled UPQC in case 1: (**a**) Responses of grid voltage v_G, compensation voltage v'_S of series transformer and load voltage v_L. (**b**) Responses of grid voltage v_{Ga}, grid current i_{Ga}, output current i_{Pa} of shunt inverter and load current i_{La}. (**c**) Responses of grid voltage v_G, compensation voltage v'_S of series transformer and load voltage v_L in the interval 9.8–10.2 s. (**d**) Responses of grid voltage v_{Ga}, grid current i_{Ga}, output current i_{Pa} of shunt inverter and load current i_{La} in the interval 9.8–10.2 s. (**e**) Responses of power angle δ, load reactive power Q_L, reactive power Q_S of series inverter, and reactive power Q_P of shunt inverter. (**f**) Response of DC-link voltage.

Finally, the most severe scenario in case 2, in which the unbalanced load $R_1 = 80\ \Omega$, $R_2 = 40\ \Omega$, $R_3 = 96\ \Omega$ is added and the linear inductive load changes from $R_{l2} = 25\ \Omega$, $L_{l2} = 30$ mH to $R_{l2} = 25\ \Omega$, $L_{l2} = 50$ mH at 4 s, is considered to evaluate the compensation performance of the developed UPQC. Meanwhile, a three-phase grid voltage sag of 20% is introduced at 10 s, and the grid voltage recovers to its nominal value at 16 s. The experimental result without using the developed UPQC in case 2 is shown in Figure 9. The responses of the line-to-line grid voltage v_{Gab}, compensation voltage v'_{Sab} of the series transformer and load voltage v_{Lab} are provided in Figure 9a. The responses of the grid voltage v_{Ga}, grid current i_{Ga}, three-phase grid current i_G, output current i_P of the shunt inverter and load current i_L are illustrated in Figure 9b. The responses of the line-to-line grid voltage v_{Gab}, compensation voltage v'_{Sab} of the series transformer and load voltage v_{Lab} in the interval 9.8–10.2 s are represented in Figure 9c. The responses of the grid voltage

v_{Ga}, grid current i_{Ga}, three-phase grid current i_G, output current i_P of the shunt inverter and load current i_L in the interval 9.8–10.2 s are shown in Figure 9d. The responses of the power angle δ, load reactive power Q_L, reactive power Q_S of the series inverter, and reactive power Q_P of the shunt inverter are provided in Figure 9e. From the experimental results, as shown in Figure 9a,d, when the three-phase grid voltage sag of 20% occurs at 10 s, the load voltage v_{Lab} also experiences a 20% sag owing to the absence of the developed UPQC. Therefore, the current-related power quality is significantly deteriorated, with a current THD of 7.6%, a lagging PF of 0.94, and a CUR of 18.6%. Consequently, the significant voltage and current-related power quality issues are observed in the absence of the developed UPQC in case 2. Moreover, the experimental result of the PI-controlled UPQC in case 2 is represented in Figure 10. The responses of the line-to-line grid voltage v_{Gab}, compensation voltage v'_{Sab} of the series transformer and load voltage v_{Lab} are provided in Figure 10a. The responses of the grid voltage v_{Ga}, grid current i_{Ga}, three-phase grid current i_G, output current i_P of the shunt inverter and load current i_L are illustrated in Figure 10b. The responses of the line-to-line grid voltage v_{Gab}, compensation voltage v'_{Sab} of the series transformer and load voltage v_{Lab} in the interval 9.8–10.2 s are represented in Figure 10c. The responses of the grid voltage v_{Ga}, grid current i_{Ga}, three-phase grid current i_G, output current i_P of the shunt inverter and load current i_L in the interval 9.8–10.2 s are shown in Figure 10d. The responses of the power angle δ, load reactive power Q_L, reactive power Q_S of the series inverter, and reactive power Q_P of the shunt inverter are provided in Figure 10e. The responses of the four-leg neutral current i_{Pn} of the shunt inverter and the neutral current i_{Ln} of the load in the interval 9.8–10.2 s are given in Figure 10f. The response of the DC-link voltage is provided in Figure 10g. According to the experimental results as shown in Figure 10a,c,d, when a 20% three-phase grid voltage sag occurs at 10 s and the grid voltage recovers to its nominal level at 16 s, the series inverter compensates for the voltage sag, thereby maintaining the load voltage v_{Lab} at its nominal level. On the other hand, the current-related power quality is mitigated, with a current THD of 3.6%, a lagging PF of 0.98, and a CUR of 3.5%. Furthermore, the shunt and series inverters each supply 50% of the load reactive power demand, as shown in Figure 10e. Then, the neutral current i_{Pn} generated by the four-leg shunt inverter effectively compensates for the load neutral current i_{Ln}, as shown in Figure 10f. In other words, the inverter neutral current is 180° out of phase with the load neutral current. However, due to the inherent limitations of the traditional PI controller, significant fluctuations in the DC-link voltage are observed when the linear inductive load is changed at 4 s, a 20% three-phase grid voltage sag occurs at 10 s, and the grid voltage recovers to its nominal level at 16 s, with corresponding settling times Δt of 124 ms, 1220 ms and 1200 ms, respectively, as shown in Figure 10g. In addition, the experimental results of the FNN and the adopted LPFNN-controlled UPQCs in case 2 are provided in Figures 11 and 12, respectively. From the experimental results, because of the merits of the adopted LPFNN controller, the current THD, lagging PF, and CUR are effectively improved to 2.9%, 0.99 and 2.7% compared with the FNN-controlled UPQC, with a current THD of 3.2%, a lagging PF of 0.99, and a CUR of 3.2% as shown in Figures 11d and 12d. Afterwards, the fluctuations in the DC-link voltage of the adopted LPFNN-controlled UPQC are also significantly suppressed at 4 s, 10 s and 16 s under grid voltage distortions and sudden load changes, and the corresponding settling times Δt are further shortened to 81 ms, 825 ms, and 815 ms, respectively, compared with the FNN-controlled UPQC, which has settling times Δt of 98 ms, 915 ms, and 955 ms, as shown in Figures 11g and 12g. Additionally, the PF, current THD, CUR, and settling time and error of the DC-link voltage using different controllers for the UPQC at 10 s in case 2 are summarized in Table 3. Therefore, in accordance with the experimental results as shown in Figures 9–12 and Table 3, the voltage and current-related power issues can be effectively mitigated by the adopted LPFNN-controlled

UPQC. Moreover, the fluctuations in the DC-link voltage are significantly suppressed under grid voltage distortions and sudden load changes, and the settling times Δt are further shortened compared with the PI- and FNN-controlled UPQCs due to the robust control and powerful computational capabilities of the adopted LPFNN controller.

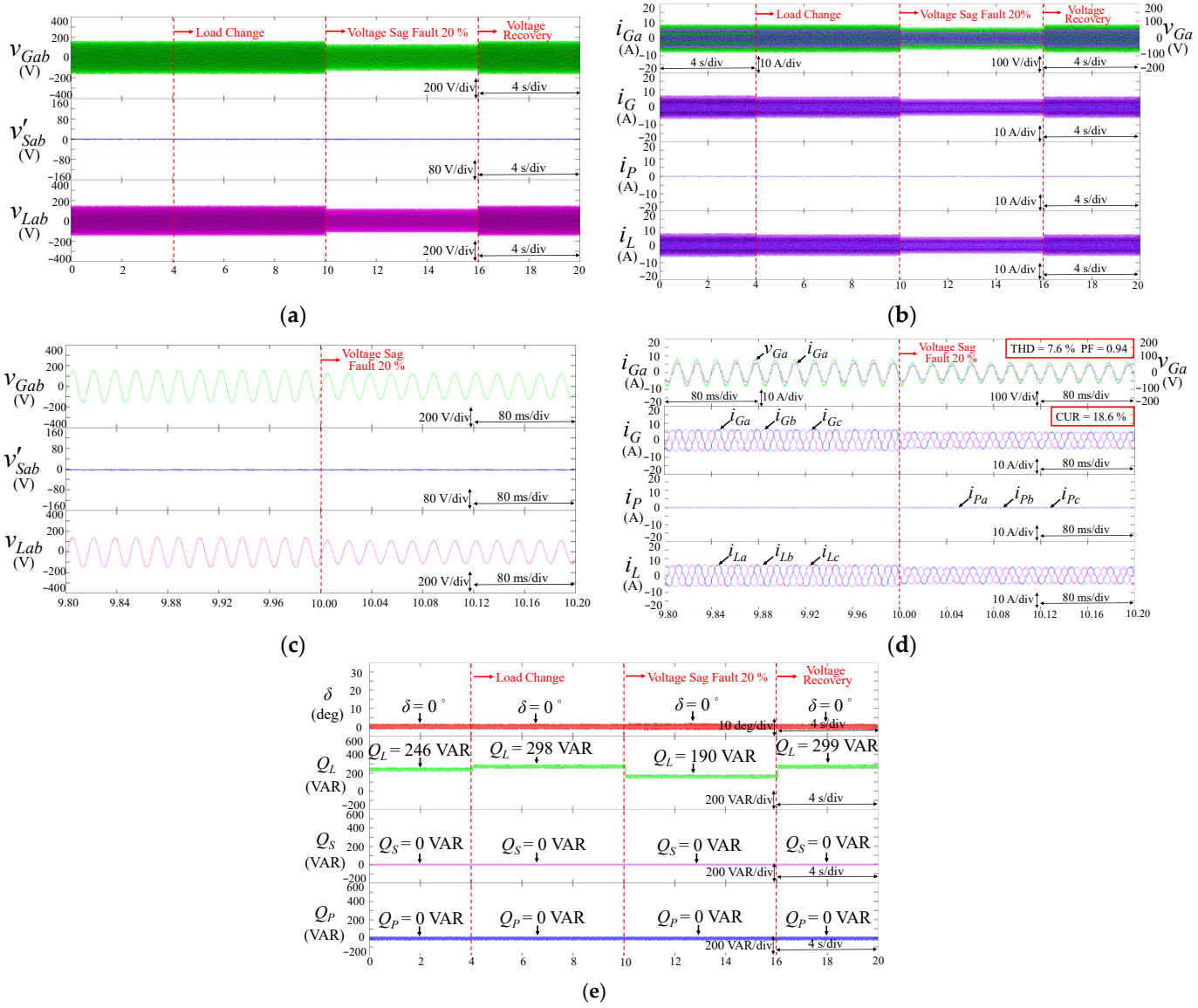


Figure 9. Experimental results without the developed UPQC in case 2: (**a**) Responses of line-to-line grid voltage v_{Gab}, compensation voltage v'_{Sab} of series transformer and load voltage v_{Lab}. (**b**) Responses of grid voltage v_{Ga}, grid current i_{Ga}, three-phase grid current i_G, output current i_P of shunt inverter and load current i_L. (**c**) Responses of line-to-line grid voltage v_{Gab}, compensation voltage v'_{Sab} of series transformer and load voltage v_{Lab} in the interval 9.8–10.2 s. (**d**) Responses of grid voltage v_{Ga}, grid current i_{Ga}, three-phase grid current i_G, output current i_P of shunt inverter and load current i_L in the interval 9.8–10.2 s. (**e**) Responses of power angle δ, load reactive power Q_L, reactive power Q_S of series inverter, and reactive power Q_P of shunt inverter.

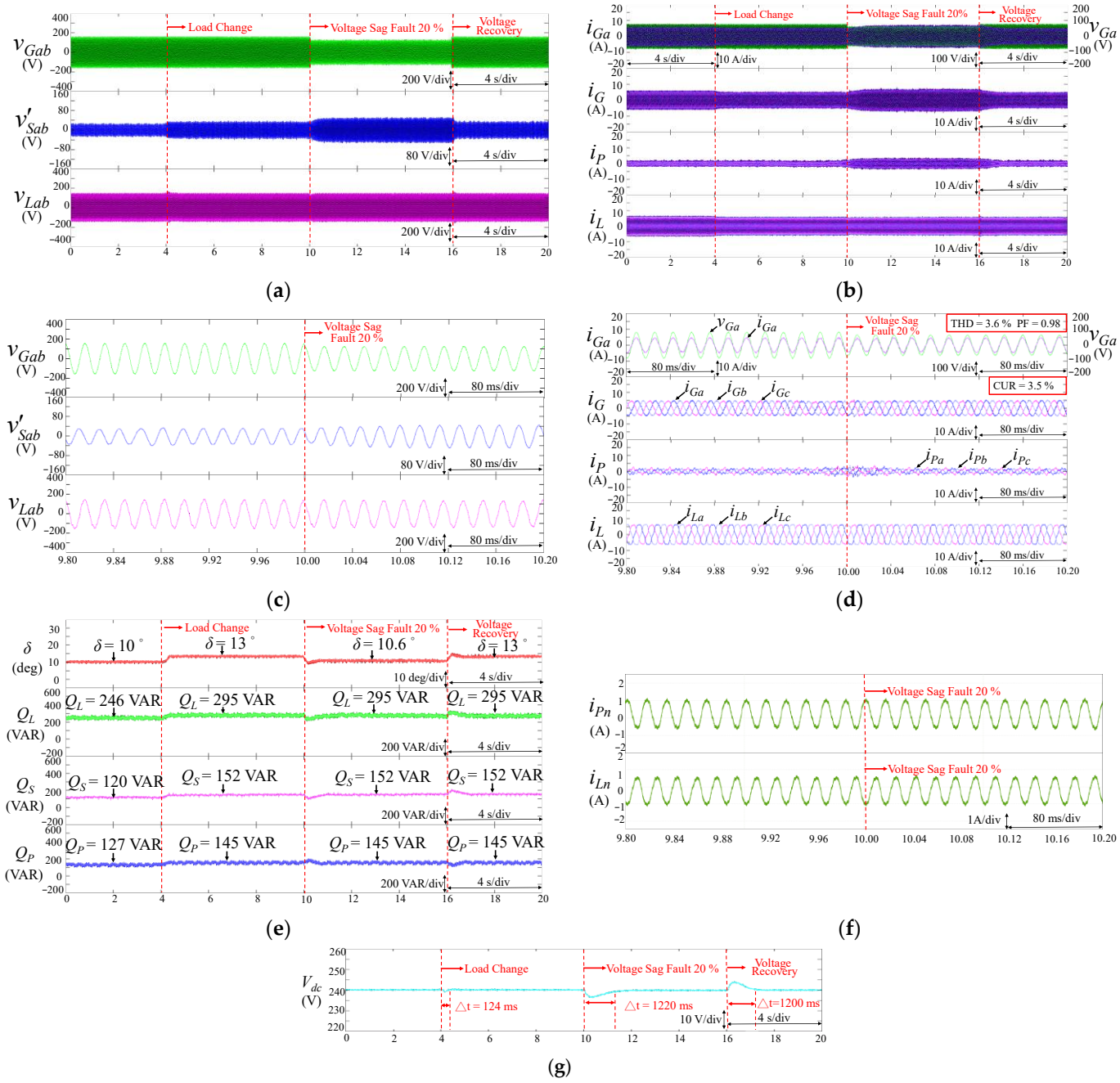


Figure 10. Experimental results of PI-controlled UPQC in case 2: (**a**) Responses of line-to-line grid voltage v_{Gab}, compensation voltage v'_{Sab} of series transformer and load voltage v_{Lab}. (**b**) Responses of grid voltage v_{Ga}, grid current i_{Ga}, three-phase grid current i_G, output current i_P of shunt inverter and load current i_L. (**c**) Responses of line-to-line grid voltage v_{Gab}, compensation voltage v'_{Sab} of series transformer and load voltage v_{Lab} in the interval 9.8–10.2 s. (**d**) Responses of grid voltage v_{Ga}, grid current i_{Ga}, three-phase grid current i_G, output current i_P of shunt inverter and load current i_L in the interval 9.8–10.2 s. (**e**) Responses of power angle δ, load reactive power Q_L, reactive power Q_S of series inverter, and reactive power Q_P of shunt inverter. (**f**) Responses of four-leg neutral current i_{Pn} of shunt inverter and neutral current i_{Ln} of load in the interval 9.8–10.2 s. (**g**) Response of DC-link voltage.

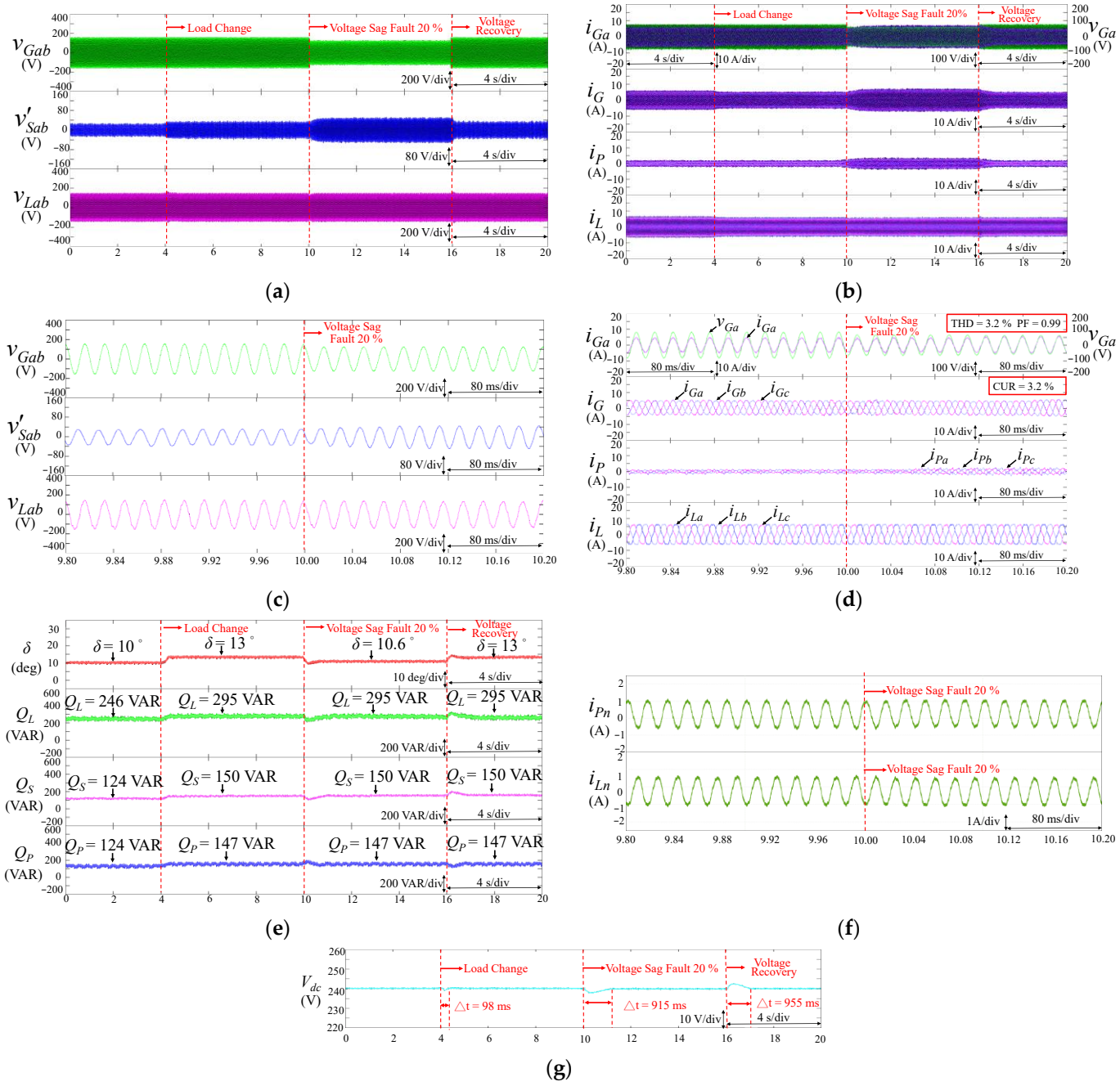


Figure 11. Experimental results of FNN-controlled UPQC in case 2: (**a**) Responses of line-to-line grid voltage v_{Gab}, compensation voltage v'_{Sab} of series transformer and load voltage v_{Lab}. (**b**) Responses of grid voltage v_{Ga}, grid current i_{Ga}, three-phase grid current i_G, output current i_P of shunt inverter and load current i_L. (**c**) Responses of line-to-line grid voltage v_{Gab}, compensation voltage v'_{Sab} of series transformer and load voltage v_{Lab} in the interval 9.8–10.2 s. (**d**) Responses of grid voltage v_{Ga}, grid current i_{Ga}, three-phase grid current i_G, output current i_P of shunt inverter and load current i_L in the interval 9.8–10.2 s. (**e**) Responses of power angle δ, load reactive power Q_L, reactive power Q_S of series inverter, and reactive power Q_P of shunt inverter. (**f**) Responses of four-leg neutral current i_{Pn} of shunt inverter and neutral current i_{Ln} of load in the interval 9.8–10.2 s. (**g**) Response of DC-link voltage.

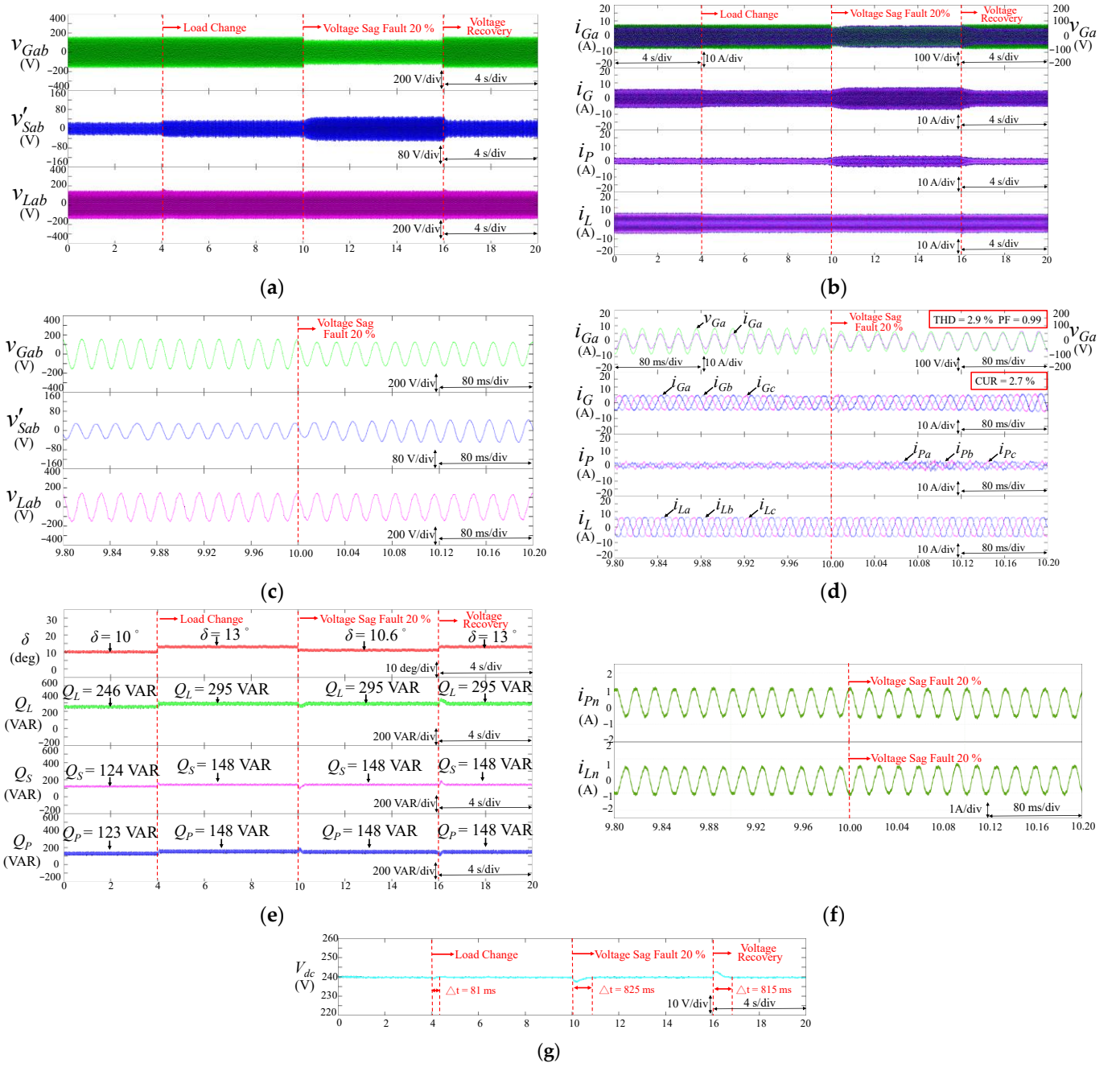


Figure 12. Experimental results of adopted LPFNN-controlled UPQC in case 2: (**a**) Responses of line-to-line grid voltage v_{Gab}, compensation voltage v'_{Sab} of series transformer and load voltage v_{Lab}. (**b**) Responses of grid voltage v_{Ga}, grid current i_{Ga}, three-phase grid current i_G, output current i_P of shunt inverter and load current i_L. (**c**) Responses of line-to-line grid voltage v_{Gab}, compensation voltage v'_{Sab} of series transformer and load voltage v_{Lab} in the interval 9.8–10.2 s. (**d**) Responses of grid voltage v_{Ga}, grid current i_{Ga}, three-phase grid current i_G, output current i_P of shunt inverter and load current i_L in the interval 9.8–10.2 s. (**e**) Responses of power angle δ, load reactive power Q_L, reactive power Q_S of series inverter, and reactive power Q_P of shunt inverter. (**f**) Responses of four-leg neutral current i_{Pn} of shunt inverter and neutral current i_{Ln} of load in the interval 9.8–10.2 s. (**g**) Response of DC-link voltage.

Table 3. PF, current THD, CUR of the grid, and settling time and error of DC-link voltage using different controllers for UPQC at 10 s in case 2.

Case Conditions	UPQC Controllers	PF	Current THD	CUR of Grid	DC-Link Voltage	
					Settling Time	Error
Case 2	None	0.94	7.6 %	18.6 %	None	None
	PI	0.98	3.6 %	3.5 %	1220 ms	4.3 V
	FNN	0.99	3.2 %	3.2 %	915 ms	3.4 V
	LPFNN	0.99	2.9 %	2.7 %	825 ms	2.6 V

In order to verify the operating performance of the online training of the network parameters of the adopted LPFNN, the waveforms of w_5^3, w_5^6, m_{13}^2, and σ_{22}^2 of the adopted LPFNN in case 2, as shown in Figure 12 for DC-link voltage control, are provided in Figure 13. According to the online learning algorithm, the parameters w_l^3, w_r^6, m_{im}^2, and σ_{im}^2 of the adopted LPFNN controller are trained online to achieve better DC-link voltage control performance. Because the powerful LPFNN controller with the DC-link voltage error $V_{dc}^* - V_{dc}$ can rapidly generate the generate the power loss I_{Loss}, the settling time of the DC-link voltage regulated by the adopted LPFNN controller can be much reduced.

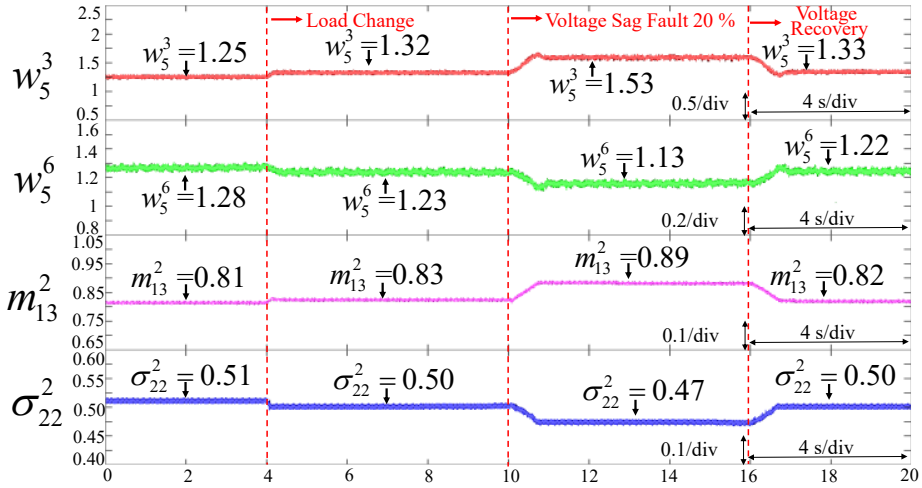


Figure 13. Responses of network parameters w_5^3, w_5^6, m_{13}^2, and σ_{22}^2 of LPFNN for DC-link voltage control.

Compared to the traditional controllers, the disadvantage of the adopted LPFNN controller is the longer execution time of the control platform. On the other hand, owing to the training process of LPFNN, the execution time of the LPFNN controller is longer than the conventional PI and FNN controllers. In this study, the execution or compute time of the "C" program in the TMS320F28335 32-bit floating-point digital signal processor (DSP) with a clock speed of 150 MHz can be obtained using the clock tool of Texas Instruments (TI) Code Composer Studio (CCS) v6 program editing interface. The total operation cycles and total execution time of the developed UPQC, using the PI, FNN and the adopted LPFNN controllers for DC-link voltage control, are compared in Table 4. The total operation cycles and total execution time for the adopted LPFNN controller are 19,167 cycles and 127.78 us respectively. As a result, the total execution time of the adopted LPFNN controller is still less than 1 ms, which is the sampling interval of the control loop.

Table 4. Execution time using PI, FNN and adopted LPFNN controllers.

Controller	PI	FNN	Adopted LPFNN
Total Operation Cycles	301	5121	19167
Execution Time	2.01 μs	34.14 μs	127.78 μs

5. Conclusions

In this study, to effectively mitigate voltage and current-related power quality issues, a three-phase four-leg intelligent UPQC is developed. The developed UPQC possesses the reactive power-sharing capability to share the load's reactive power demand between the series and shunt inverters. Moreover, to suppress fluctuations in the DC-link voltage under grid voltage distortions and sudden load changes, the LPFNN controller is employed in place of the traditional PI and FNN controllers for DC-link voltage control and power quality improvement. Furthermore, according to the experimental results, the developed LPFNN-controlled UPQC can effectively achieve improved PF, current THD, VUR, CUR, and DC-link voltage regulation performance, including shorter settling times and smaller errors, under grid voltage distortions and sudden load changes compared with the traditional PI- and FNN-controlled UPQCs, owing to the robust control and powerful computational capabilities of the adopted LPFNN controller.

Author Contributions: Conceptualization, K.-H.T. and F.-J.L.; methodology, K.-H.T.; software, W.-M.L.; validation, C.-M.S., W.-M.L. and P.-C.T.; formal analysis, C.-M.S. and W.-M.L.; investigation, C.-M.S. and W.-M.L.; resources, W.-M.L. and C.-C.L.; data curation, C.-M.S., P.-C.T. and C.-C.L.; writing—original draft, K.-H.T.; writing—review & editing, K.-H.T. and F.-J.L.; visualization, P.-C.T.; supervision, F.-J.L.; project administration, C.-C.L. All authors have read and agreed to the published version of the manuscript.

Funding: This research was funded by the National Science and Technology Council of Taiwan, grant number NSTC 115-2221-E-606-007.

Data Availability Statement: The original contributions presented in this study are included in the article. Further inquiries can be directed to the corresponding author.

Conflicts of Interest: Chia-Ching Lin was employed by the R&D Center, Fortune Electric Co., Ltd. The remaining authors declare that the research was conducted in the absence of any commercial or financial relationships that could be construed as a potential conflict of interest.

References

1. Lin, F.J.; Tan, K.H.; Kuan, Z.Y.; Wang, C.Y. Droop Controlled Microgrid with Intelligent PV-DSTATCOM for Power Quality Improvement. *IEEE Trans. Power Electron.* **2025**, *40*, 12754–12769. [CrossRef]
2. Al-Gahtani, S.F.; Barnawi, A.B.; Azazi, H.Z.; Irshad, S.M.; Bhutto, J.K.; Mahammad, M.H.; Salem, E.Z.M. A New Technique Implemented in Synchronous Reference Frame for DVR Control Under Severe Sag and Swell Conditions. *IEEE Access* **2022**, *10*, 25565–25579. [CrossRef]
3. Fu, W.; Wang, Q.; Hua, W.; Cheng, M.; Buja, G. A Simplified Cost-Effective DuC-UPQC with Multiobjective Optimization Design. *IEEE Trans. Power Electron.* **2026**, *41*, 8595–8611. [CrossRef]
4. Tan, K.H.; Li, Y.R.; Lee, Y.D.; Wang, S.S. Dynamic Voltage Restorer Using Intelligent CPFNN to Mitigate Abnormal Grid Voltage for Loads. *IEEE J. Emerg. Sel. Top. Power Electron.* **2025**, *13*, 6322–6335. [CrossRef]
5. Khadkikar, V. Enhancing Electric Power Quality Using UPQC: A Comprehensive Overview. *IEEE Trans. Power Electron.* **2012**, *27*, 2284–2297. [CrossRef]
6. Tan, K.H.; Chen, J.H.; Lee, Y.D. Intelligent Controlled Dynamic Voltage Restorer for Improving Transient Voltage Quality. *IEEE Access* **2023**, *11*, 74686–74701. [CrossRef]

7. Özer, A.S.; Sevilmiş, F.; Karaca, H.; Ahmed, H. Power Quality Improvement of DSTATCOM Using Fast Hybrid-PLL-based Control Method for Wind Energy Applications. *Prot. Control Mod. Power Syst.* **2026**, *11*, 16–34. [CrossRef]
8. Sanjenbam, C.D.; Singh, B. PQ Improvement of Four Wire Distribution Grid Based Dual Stage Solar PV Array Integrated UPQC. *IEEE J. Emerg. Sel. Top. Ind. Electron.* **2026**, *7*, 80–89. [CrossRef]
9. Ray, P.; Ray, P.K. Performance Enhancement of PV-UPQC with Integration of Battery Energy Storage System at the DC-Link to Support Sensitive Consumer Loads. *IEEE Trans. Consum. Electron.* **2024**, *70*, 6496–6506. [CrossRef]
10. Kumar, D.; Hrishikesan, V.M.; Deka, A.K.; Das, D.; Kumar, C.; Mishra, M.K. A Meshed Hybrid Microgrid Configuration with Unified Power Quality Conditioner. *IEEE J. Emerg. Sel. Top. Power Electron.* **2025**, *13*, 2489–2499. [CrossRef]
11. Jia, W.; Guo, Q.; Tu, C.; Jiang, F.; Wang, L.; Hou, Y. Improved Single-Phase UPQC with Integrating Auxiliary Capacitor for Power Rating Reduction. *IEEE Trans. Ind. Electron.* **2023**, *70*, 9091–9102. [CrossRef]
12. Wang, G.; Jiang, Y.; Liu, Z.; Ma, Y.; Wang, J. Predictive Direct Control of Nine-Switch Converter Unified Power Quality Conditioner Based on Time-Sharing Cooperative Control. *IEEE Trans. Power Electron.* **2025**, *40*, 5895–5906. [CrossRef]
13. Srilakshmi, K.; Balachandran, P.K.; Zainuri, M.A.A.M. Osprey Optimization Algorithm-Based Power Quality Enhanced Grid Interfaced Green Energy Fed Electric Vehicle Charging for Industrial/House Hold Consumers. *IEEE Trans. Consum. Electron.* **2026**, *72*, 1011–1025. [CrossRef]
14. Cardoso, J.T.; Jacobina, C.B.; Felinto, A.S.; dos Santos Júnior, A.A.; Corrêa, M.B.R. Single-Phase Transformerless Unified Power Quality Conditioner Based on Three-Leg and Standby Converters. *IEEE Trans. Ind. Appl.* **2025**, *61*, 9481–9492. [CrossRef]
15. Jiang, C.; Yuan, C.; Wang, F.; Zhang, S. Coordinated Direct Power Strategy Based Active Disturbance Rejection Control for MMC-UPQC. *IEEE Trans. Ind. Electron.* **2025**, *72*, 11778–11790. [CrossRef]
16. Ambati, B.B.; Khadkikar, V. Optimal Sizing of UPQC Considering VA Loading and Maximum Utilization of Power-Electronic Converters. *IEEE Trans. Power Del.* **2014**, *29*, 1490–1498. [CrossRef]
17. Li, Z.; Yang, R.; Zhou, Y.; Wang, C.; Wang, Z. A Unified Framework for Adaptive and Flexible Phase Angle Regulation in Single-Phase UPQC. *IEEE Trans. Power Electron.* **2025**, *40*, 12779–12793. [CrossRef]
18. Khadkikar, V.; Chandra, A. UPQC-S: A Novel Concept of Simultaneous Voltage Sag/Swell and Load Reactive Power Compensations Utilizing Series Inverter of UPQC. *IEEE Trans. Power Electron.* **2011**, *26*, 2414–2425. [CrossRef]
19. Meng, L.; Ma, L.; Zhu, W.; Yan, H.; Wang, T.; Mao, W.; He, X.; Shu, Z. Control Strategy of Single-Phase UPQC for Suppressing the Influences of Low-Frequency DC-Link Voltage Ripple. *IEEE Trans. Power Electron.* **2022**, *37*, 2113–2124. [CrossRef]
20. Kong, L.; Tang, H.; Wu, C.; Wang, J.; Wu, P.; Wang, Y.; Blaabjerg, F. Analysis and Damping of Subsynchronous Oscillations for Cascaded Grid-Forming Converters Considering DC-Link Dynamics. *IEEE Trans. Power Electron.* **2025**, *40*, 2284–2299. [CrossRef]
21. Tan, K.H.; Li, M.Y.; Weng, X.Y. Droop Controlled Microgrid with DSTATCOM for Reactive Power Compensation and Power Quality Improvement. *IEEE Access* **2022**, *10*, 121602–121614. [CrossRef]
22. Ahmed, H.; Çelik, D. Enhanced UPQC Control Scheme for Power Quality Improvement in Wave Energy Driven PMSG System. *IEEE Trans. Energy Convers.* **2025**, *40*, 246–257. [CrossRef]
23. Kinhal, V.G.; Agarwal, P.; Gupta, H.O. Performance Investigation of Neural-Network-Based Unified Power-Quality Conditioner. *IEEE Trans. Power Del.* **2011**, *26*, 431–437. [CrossRef]
24. Halbouni, A.; Gunawan, T.S.; Habaebi, M.H.; Halbouni, M.; Kartiwi, M.; Ahmad, R. Machine Learning and Deep Learning Approaches for CyberSecurity: A Review. *IEEE Access* **2022**, *10*, 19572–19585. [CrossRef]
25. Tomaras, D.; Buschjäger, S.; Kalogeraki, V.; Morik, K.; Gunopulos, D. STRATA2.0: A Serverless Middleware for Machine Learning Training. *IEEE Trans. Parallel Distrib. Syst.* **2026**, *37*, 1872–1884. [CrossRef]
26. Yang, Y.; Zhou, C.; Zhang, H.; Peng, Y.; Sun, H. Denoising CSEM Data Using Least-Squares Method Based on Mixed Basis of Fourier Series and Legendre Polynomials. *IEEE Trans. Geosci. Remote Sens.* **2023**, *61*, 5921812. [CrossRef]
27. Chen, J.; Xu, L. Improved Modeling and Generalization Capabilities of Graph Neural Networks with Legendre Polynomials. *IEEE Access* **2023**, *11*, 63442–63450. [CrossRef]
28. Song, J.; Liu, G.; Tang, Y.; Wang, L.; Wang, M.; Li, L. An Innovative Formal Verification Method Based on Timed Petri Nets with Integrated Database Tables. *IEEE Trans. Syst. Man. Cybern. Syst.* **2025**, *55*, 7410–7424. [CrossRef]
29. Liu, S.; Oh, S.K.; Pedrycz, W.; Yang, B.; Wang, L.; Yoon, J.H. Reinforced Interval Type-2 Fuzzy Clustering-Based Neural Network Realized Through Attention-Based Clustering Mechanism and Successive Learning. *IEEE Trans. Fuzzy Syst.* **2024**, *32*, 1208–1222. [CrossRef]
30. Wang, Y.; Zhao, P.; Sun, J. Recurrent Neural Network Based on DNA Strand Displacement Circuits and Its Application in Location Prediction. *IEEE Trans. Nanobiosci.* **2026**, *25*, 349–360. [CrossRef] [PubMed]
31. Yoo, S.J.; Choi, Y.H.; Park, J.B. Generalized Predictive Control Based on Self-recurrent Wavelet Neural Network For Stable Path Tracking of Mobile Robots: Adaptive Learning Rates Approach. *IEEE Trans. Circuits Syst. I-Regul. Pap.* **2006**, *53*, 1381–1395. [CrossRef]

32. Wai, R.J.; Li, C.M. Design of Dynamic Petri Recurrent Fuzzy Neural Network and Its Application to Path-tracking Control of Nonholonomic Mobile Robo. *IEEE Trans. Ind. Electron.* **2009**, *56*, 2667–2683. [CrossRef]
33. *IEEE Standard 1159-2019*; IEEE Recommended Practice for Monitoring Electric Power Quality. IEEE: Piscataway, NJ, USA, 2019.

Disclaimer/Publisher's Note: The statements, opinions and data contained in all publications are solely those of the individual author(s) and contributor(s) and not of MDPI and/or the editor(s). MDPI and/or the editor(s) disclaim responsibility for any injury to people or property resulting from any ideas, methods, instructions or products referred to in the content.